JOURNAL OF GEOPHYSICAL RESEARCH: PLANETS, VOL. 118, 1915–1933, doi:10.1002/jgre.20145, 2013

Ground penetrating radar geologic field studies of the ejecta of Barringer Meteorite Crater, Arizona, as a planetary analog

Patrick S. Russell,[1] John A. Grant,[1] Kevin K. Williams,[2] Lynn M. Carter,[3] W. Brent Garry,[3] and Ingrid J. Daubar[4]

Received 23 May 2013; revised 9 August 2013; accepted 27 August 2013; published 23 September 2013.

[1] Ground penetrating radar (GPR) has been a useful geophysical tool in investigating a variety of shallow subsurface geological environments on Earth. Here we investigate the capabilities of GPR to provide useful geologic information in one of the most common geologic settings of planetary surfaces, impact crater ejecta. Three types of ejecta are surveyed with GPR at two wavelengths (400 MHz, 200 MHz) at Meteor Crater, Arizona, with the goal of capturing the GPR signature of the subsurface rock population. In order to "ground truth" the GPR characterization, subsurface rocks are visually counted and measured in preexisting subsurface exposures immediately adjacent to and below the GPR transect. The rock size-frequency distribution from 10 to 50 cm based on visual counts is well described by both power law and exponential functions, the former slightly better, reflecting the control of fragmentation processes during the impact-ejection event. GPR counts are found to overestimate the number of subsurface rocks in the upper meter (by a factor of 2–3x) and underestimate in the second meter of depth (0.6–1.0x), results attributable to the highly scattering nature of blocky ejecta. Overturned ejecta that is fractured yet in which fragments are minimally displaced from their complement fragments produces fewer GPR returns than well-mixed ejecta. The use of two wavelengths and division of results into multiple depth zones provides multiple aspects by which to characterize the ejecta block population. Remote GPR measurement of subsurface ejecta in future planetary situations with no subsurface exposure can be used to characterize those rock populations relative to that of Meteor Crater.

Citation: Russell, P. S., J. A. Grant, K. K. Williams, L. M. Carter, W. Brent Garry, and I. J. Daubar (2013), Ground penetrating radar geologic field studies of the ejecta of Barringer Meteorite Crater, Arizona, as a planetary analog, *J. Geophys. Res. Planets*, *118*, 1915–1933, doi:10.1002/jgre.20145.

1. Introduction

[2] Ground penetrating radar (GPR) studies can yield insight into the physical properties, rock-size distribution, structure, and layering in the shallow subsurface, thereby granting a three-dimensional view of the processes affecting an area over geologic time. The broad motivation and implications of the present work relate to how GPR data from terrestrial analogs can help constrain models for evolution of the lunar and martian surface, aid in interpretation of orbital SAR or radar sounding data, and help predict what might be encountered in the subsurface during future landed scientific or engineering operations on the Moon or Mars.

[3] Broadly speaking, GPR data consist of radar pulses returned from the subsurface, where two main factors influence and modify the propagation of waves, contributing their fingerprint to the final radargram: a material's dielectric properties (e.g., electric conductivity, magnetic susceptibility, typically linked to composition) and subsurface structure, or arrangement of different materials (e.g., layering, discrete objects). Our goal is to characterize the structure of the subsurface with GPR and to use this GPR characterization to constrain geological process. While the determination of subsurface dielectric can inform composition and performance of GPR in one environment compared to another (e.g., another planet's surface) is dependent on relative dielectrics, these aspects of study are not subjects of this geologic-process focused work, although they are discussed below. Our study's approach draws on the rationale that fundamentally different processes (e.g., impact ejection, volcanism, fluival transport) produce characteristic deposits with certain physical properties that are, in some way(s), diagnostic of the process. Investigation and documentation

[1]Center for Earth and Planetary Studies, National Air and Space Museum, Smithsonian Institution, MRC 315, Washington DC, USA.
[2]Department of Earth Sciences and Science Education, SUNY-Buffalo State, Buffalo, New York, USA.
[3]NASA-Goddard Spaceflight Center, Greenbelt, Maryland, USA.
[4]Department of Planetary Sciences, Lunar, and Planetary Lab, University of Arizona, Tucson, Arizona, USA.

Corresponding author: P. S. Russell, Center for Earth and Planetary Studies, National Air and Space Museum, Smithsonian Institution, MRC 315, PO Box 37012, Washington DC 20013, USA. (russellp@si.edu)

2169-9097/13/10.1002/jgre.20145

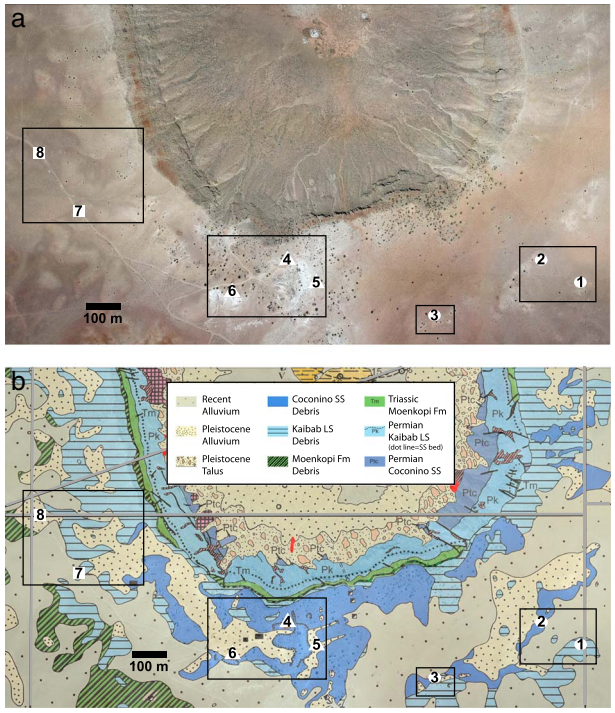

Figure 1. Southern portion of Meteor Crater and surrounding ejecta. (a) Background image from GoogleEarth. Light toned lobes are low mounds of ejecta; darker reddish tones are generally intervening low areas more covered with fines and soil. Bright white areas directly south are exposures of defunct silica mine. (b) Geologic map based on *Shoemaker* [1960] as reproduced by *Kring* [2007], with simplified legend of most pertinent materials. Box outlines and white markers indicate specific GPR study sites (numbered) which are enlarged in Figures 4a–4c: Circles = Lobe ejecta sites; Triangles = Quarry ejecta sites; Squares = Trail ejecta sites.

of the structure-dominated characteristics of the GPR signature produced by these different deposits in known settings will aid recognition of such deposits in remote settings and thus assist in the distinction between fundamental processes that have influenced those settings.

[4] One of the major challenges in using GPR in geologic investigations is the degree to which structures and features of the subsurface can be uniquely, distinctly, and directly identified. We recognize that the complexities of radar wave interaction with intricate and unknown subsurface structures and configurations of materials in the real world often result in complex radargrams in which it may not be straightforward or possible to directly account for every feature ("wiggle," line, curve) in the radargram, or to identify or pinpoint the precise subsurface structure or property causing it. This is likely to be true especially in blocky, regolith-like subsurfaces, in which the ideal case of an isolated object in a homogeneous background producing "text-book" return patterns may not be realized. Cognizant of this common inherent limitation, we demonstrate that GPR can be used to glean information on the subsurface that is nevertheless useful in characterizing and interpreting the geologic environment. As mentioned above, the basis for this approach is that different geological processes produce deposits that are inherently reflective of that process. If GPR can consistently characterize the subsurface produced by a particular process, then this characterization may serve as a signature by which to distinguish these deposits from amongst GPR measurements of deposits produced by other fundamental processes. In recognition of the complexities imparted to real-world radargrams by a subsurface with many object scatterers, the GPR characterization, or signature, does not necessarily have to illuminate the exact nature and configuration of objects and materials in the subsurface. Rather, it must at least provide some metric deriving directly from the bulk properties and configuration of the subsurface that is repeatable for that type of deposit and different from deposits of other origin. We directly link the GPR signature to the real subsurface geology, in particular the volumetric density of ejecta blocks in the subsurface, by comparing it with "ground-truth" observations of subsurface exposures immediately adjacent or subjacent to our GPR transects.

[5] In this work, we describe the characterization of the GPR signature of a fresh terrestrial impact crater: Barringer Meteorite Crater (hereafter Meteor Crater), Arizona, USA (Figure 1a). Impact cratering is one of the dominant processes in planetary surface modification, and, hence, craters and their ejecta are perhaps the most prevalent feature of the lunar and martian surfaces. Results of this study will serve as a basis of comparison of GPR expression of impact ejecta to that of other planetary analog terrains such as lava flows, cinders, flood deps [e.g., *Russell et al*., 2012; *Khan et al*., 2007].

[6] Most of our understanding of the Moon and Mars is based on surface data collected by orbiter and landed missions. Relatively little is known about the subsurface, as missions focusing on digging and drilling have so far been limited in extent on the Moon and prohibitively expensive. Because GPR is an efficient, noninvasive tool with which measurements over a wide area can be made relatively quickly and easily (as compared to coring or excavation), it is well suited to future exploration of the lunar and martian subsurface and could extend results from cores or outcrops over much greater areas than otherwise possible. GPR is capable of addressing a wide range of geological questions pertaining to the near surface of terrestrial planets, as demonstrated over the last several decades in scientific investigations and engineering applications of both terrestrial [e.g., *Mellet*, 1995; *Dominic et al*., 1995; *Benson*, 1995; *Milsom*, 2003; *Mussett and Khan*, 2000; *Jol*, 2009; *Baker and Jol*, 2007; Geophysical Survey Systems, Inc.: www.geophysical.com/gssidocumentation.htm, "Case Studies" tab] and planetary-analog [e.g., *Paillou et al*., 2001; *Fukui et al*., 2008; *Bristow et al*., 2010; *Grant et al*., 2004; *Heggy and Paillou*, 2006; *Degenhardt and Giardino*, 2003; *Khan et al*., 2007; *Grant and Schultz*, 1994; *Unrau et al*., 2010; *Dinwiddie et al*., 2011; *Hooper et al*., 2012] focus.

[7] GPR has not yet been employed on the surface of another planet, but would assist in achieving a range of science objectives set forth by the Mars and Moon Exploration Analysis Groups [*MEPAG*, 2008; *Shearer et al*., 2004; *LEAG*, 2009a, 2009b]. GPR instrumentation has been explicitly pursued, discussed, and recommended for inclusion in missions to Mars in the past [e.g., *Berthelier et al*., 2003; *Grant et al*., 2001; *Grant et al*., 2003; *Vannaroni et al*., 2004; *Leuschen et al*., 2003a; *Olhoeft*, 1998], has been tested in rover operations [*Furgale*

et al., 2010; *Graham et al*., 2013], and is included in the current instrument payload of the ESA's ExoMars mission [Water Ice Subsurface Deposit Observation on Mars (WISDOM) GPR; *Ciarletti et al*., 2011]. Results from the present study will also: (1) directly support ongoing and future development of effective planetary GPR instrumentation, deployment, and field-campaign design; and (2) contribute toward constraining the geology in the interpretation of data collected remotely from the Moon or Mars.

2. Background

2.1. GPR

[8] The GPR equipment employed in this study comprises a 400 MHz transceiver (an antenna that is both the emitter and receiver of signal), a 200 MHz transceiver, an SIR-3000 GPR data control and recording system, and a survey wheel for measuring distance, all from Geophysical Survey Systems International (GSSI). Numerous sources review GPR principles and operation [e.g., *Jol*, 2009; *Conyers*, 2004, *Daniels*, 2007; *Baker et al*., 2007], from which salient topics are briefly introduced here. Impulse ground penetrating radar involves sending pulses of electromagnetic radiation into the subsurface and measuring the timing and strength of the return signals. Sending hundreds or thousands of consecutive pulses and waiting successively longer time intervals at which to record the return power successively build up a 1-D vertical scan trace from shallow to deeper depths. Repeating this scan sequence as the antenna is dragged across the surface builds a two-dimensional profile, or radargram, of time-depth scan traces along the transect. To maximize the power transmitted into and received from the subsurface, the antenna should be in constant and uniform contact with the ground surface as it is dragged along the transect. Propagating power is dissipated along its path largely according to the material's dielectric permittivity, ε (here understood to be relative to that of air), resulting in an exponential decay of signal strength with depth. Typically, for nonwet geological materials, ε = ~3–11. Higher dielectric permittivity also decreases the speed of the waves in the medium, shortening their effective wavelength. The velocity of waves in the ground is:

$$v_g = c/\sqrt{\varepsilon} \tag{1}$$

where c = speed of light, and v_g = radar wave velocity in the ground.

[9] The wavelength in the ground, λ_g, is:

$$\lambda_g = v_g/f_c \tag{2}$$

where f_c = the GPR center frequency.

[10] For example, while a 400 MHz antenna produces a wavelength of 0.75 m in air, the wavelength would become 38 cm in material with ε = 4 and 25 cm in material with ε = 9. Transmitted signal is reflected when it encounters a change in dielectric permittivity of the subsurface through which it is traveling. Such interfaces may come in the form of layers, material transitions, or an embedded object, due to changes in density, porosity (filled with air or water), salinity, acidity, or composition, for example. The presence of groundwater, clays, sulfates, or carbonates greatly attenuates radar signal passing through them due to the contribution of their conductive properties to a higher dielectric permittivity. Highly conductive materials, such as metals and salt water, appear highly reflective and effectively prohibit the passage of GPR signal. Iron-bearing minerals or soils affect a material's magnetic permeability, which also increases signal attenuation and decreases velocity. Thus, the components of the subsurface significantly control the propagation of radar waves and the maximum depth of penetration. It is generally considered that the absence of liquid water in planetary near surfaces, within subsurface pore space or as films on regolith grains, could result in vastly improved propagation performance over that typical on Earth. However, several studies have indicated that the presence of iron-bearing phases in grains, dust, and rocks on Mars may dampen such expectations and deserve close consideration [e.g., *Paillou et al*., 2001; *Heggy et al*., 2001; *Stillman and Olhoeft*, 2008; *Williams and Greeley*, 2004; *Pettinelli et al*., 2006]. In addition, some knowledge of subsurface dielectric properties is necessary to convert the timing of a return in a scan trace to depth (length) units.

[11] The wave transmitted from a GPR antenna is propagated into a volume of subsurface over which the strength of signal varies with direction, with a nadir-focused central cone of highest power and side lobes of significantly less importance. The angular width of the central beam concentration at half maximum power of our antenna is roughly 60° in air (GSSI personal communication), but the divergence decreases as the signal travels through materials of higher dielectric permittivity.

[12] The measured returned signal is the integrated power returned to the antenna from all directions at a given time. Because the sampled volume of subsurface extends along a transect both ahead and behind nadir as well as to the sides, the GPR "sees" a reflection caused by a buried object further ahead in the transect before being positioned directly over the object. As the GPR advances along the surface transect, the direct-line distance to the object ahead decreases, reaching a minimum when the GPR is directly over it. This scenario produces an apparently rising reflector in the 2-D data profile being gathered, as the reflected returns are detected sooner during approach as the straight-line distance decreases. The opposite geometric progression unfolds as the GPR moves away along the transect having passed over the object, producing an apparently descending reflector in the radargram. The result is a return in the shape of a convex-up hyperbola, with the actual location of the buried object at its apex.

[13] GPR is characterized as an ultra-wideband radar, in which the ratio of the bandwidth to center frequency is close to one, i.e., a 400 MHz GPR has a bandwidth of ~400 MHz, producing a signal with frequencies from 200 MHz to 600 MHz with the most emitted power concentrated around 400 MHz. The temporal pulse width, τ, is the inverse of the bandwidth, 2.5 ns for a 400 MHz GPR. The resolution of GPR in the along-propagation direction, Δr, is generally considered to be the ground separation distance of two boundaries equivalent to a temporal separation of one half of the pulse width in the data, closer than which the two returned signals would be indistinguishable. If two pulses are τ/2 ns apart in the two-way travel time data, the interfaces that produced them are the equivalent of τ/4 ns apart in the ground, so:

$$\Delta r = v_g \tau/4 \tag{3}$$

which, for a 400 MHz GPR, is 19 cm in air, 9 cm with ε = 4, and 6 cm with ε = 9. In order to distinguish laterally separated

objects at a given depth, d, by τ/2 ns in the radargram requires a lateral resolution, Δl, of:

$$\Delta l = \sqrt{v_g d\tau/2} \quad (4)$$

which, for a 400 MHz GPR at a depth of 1 m, is 61 cm in air, 43 cm with ε = 4, and 35 cm with ε = 9. Equation 4 is also the formula for the radius of the radiation footprint of the descending radar waves (actually more elliptical than circular) as represented by the cross-sectional area of the first Fresnel zone around a propagating wave, generally taken to be an approximation of the area of radar illumination at a given depth. Objects at or above the scale of one quarter of this area (half of the length) are likely to contribute significantly to the return signal; objects much smaller than this are likely not to be well registered by the passing waves.

[14] Because radar waves propagate into a volume of the subsurface, the radargram is not a true 2-D profile—it reflects a zone of subsurface along the transect that has some width. The width of this zone increases with depth but at a decreasing rate. We take the width represented by a scan trace, constant along the 2-D profile, to be one Fresnel radius on either side of nadir. Integrating width over depth, the area of this transect-perpendicular slice is multiplied by the transect length to obtain the transect volume from which the GPR returns are registered.

[15] While the above estimations of GPR behavior such as propagation, reflection, resolution, and sample volume are based on ideal physical situations, they enable geologic interpretations to be made. The physical characteristics of the natural subsurface are often too heterogeneous and complex to precisely reconstruct with GPR.

2.2. Meteor Crater

[16] Meteor Crater is chosen as an analog because it is an accessible, fresh crater and has been used in planetary analog studies for decades [e.g., *Shoemaker*, 1960, 1963; *Roddy et al*., 1975; *Kumar et al*., 2010]. Meteor Crater is a ~1.2 km diameter basin excavated by the impact of an iron meteorite into the relatively smooth surface of flat-lying Permo-Triassic sedimentary rocks of the Colorado Plateau Sequence [*Barringer*, 1905; *Shoemaker*, 1960, Figure 1b]. The generalized stratigraphy of units intersected by the crater and present in its ejecta comprises the ~220 m thick Permian Coconino sandstone, the ~80 m thick Permian Kaibab dolomite, and the ~9 m thick Triassic Moenkopi sand- and siltstone. The Coconino is a bright white, very pure (~97% silica) sandstone characterized by aeolian cross-bedding, the laminae of which are often visible in ejecta blocks. The Kaibab is a light yellow, generally microcrystalline, fossiliferous marine dolomite with interspersed beds of higher-silica calcareous sandstone. The Moenkopi contains more lithologic variety due to its origin as a coastal floodplain, including sandstones, siltstones, and occasionally shale. The unit contains fossils and tracks indicative of the depositional environment. The bulk of the sediments are moderately silicious and calcareous and are stained strikingly rust-red as the result of a significant iron content. For further detail on the geological and historical context of Meteor Crater, see the excellent review by *Kring* [2007] and references therein.

[17] The ejecta deposits of Meteor Crater have been mapped and studied extensively [e.g., *Shoemaker*, 1960, 1963; *Shoemaker and Kieffer*, 1974; *Roddy et al*., 1975; *Kring*, 2007]. The continuous overturned ejecta blanket extends ~1.3–1.9 km from the crater rim [*Roddy et al*., 1975] while individual blocks have been found up to 6 km away [*Gilbert et al*., 1896]. The raised crater rim slopes outward at just under 20° for ~100 m, of which the entire present surface is ejecta material. Exterior to this, the current surface exposure of ejecta, sloping at an average of ~5°, becomes more discontinuous, in the form of low mounds, or lobes, of ejecta among intervening areas of smooth, postimpact alluvium and colluvium. Ejecta fragments at lobe margins that have moved downslope may be interfingering with the alluvium. Net erosion on the upper rim has been estimated at ~9 m [*Nishiizumi et al*., 1991] and up to 20 m [*Shoemaker and Kieffer*, 1974]. GPR-derived relationships of ejecta and surrounding sediments on the lower rim were used by *Grant and Schultz* [1994] to verify postimpact erosion [*Grant and Schultz*, 1993] of ~≤1 m, with local concentrated erosion of 2–3 m.

3. Approach and Methods

[18] Our primary goal is to characterize the subsurface structure of impact ejecta at Meteor Crater with GPR. The metric we use is the apparent number, or volumetric density, of blocks apparent in the radargrams. By comparing these radargram counts with visual measurements of block number, size, and depth at an adjacent, preexisiting outcrop exposure, we obtain the relationship between the apparent block distribution in the radar data and the actual, outcrop-derived block population. Collecting data at two frequencies (200 MHz and 400 MHz) allows assessment of how GPR detections (e.g., number and depth) vary with the wavelength of the antenna employed, giving two aspects to the metric with which to characterize the radar block distribution. Comparison of future GPR data from impact settings where no subsurface exposure is available with results from Meteor Crater will allow estimation of the relative (to Meteor Crater) near-surface blockiness at those sites.

[19] Our study is concerned with GPR-based geologic interpretations, differing from field studies focusing on specific terrestrial conditions that most fully replicate a particular planetary dielectric environment or aim to determine geophysical parameters of analog subsurface materials [e.g., *Paillou et al*., 2001; *Thomson et al*., 2012; *Heggy et al*., 2006a, 2006b]. Planetary dielectrics can be estimated based on knowledge of earth materials but are hard to predict for specific local planetary sites. Furthermore, on Earth, it is rare to get a good natural field analog to dielectric properties of planetary surfaces, due to prevalence and varying states of water, clays, evolved (e.g., granitic) and biogenic and water-derived (e.g., carbonate) lithologies. In fact, the site of Meteor Crater is likely to be a poor dielectric analog to the lunar or martian surface, where surfaces are largely volcanically derived, due to the prevalence of carbonate and quartzite lithologies. Therefore, we are not measuring, or using as an analog, the dielectric properties at our site to gain direct knowledge of planetary dielectric properties, nor are we comparing the dielectric properties of our sites directly against those of planetary surfaces.

[20] In any environment, the representation of the subsurface medium with a single dielectric value clearly oversimplifies the dielectric variability. The value of subsurface dielectric used,

Table 1. GPR Data Collected at Each Numbered Site Within Three Ejecta Types Along Southern Rim of Meteor Crater[a]

Site	Field Seasons	Transect Lines	GPR Data Transects Collected	
			400 MHz	200 MHz
		Lobe Ejecta		
1	J, O, A	12	17	7
2	O	3	6	6
3	J	1	3	2
		Quarry Ejecta		
4	O	2	6	4
5	O	2	6	3
6	J	1	2	2
		Trail Ejecta		
7	A	1	3	4
8	A	1	4	4

[a]Individual transect lines depicted in Figures 4a–4c; in many cases, multiple data-collection passes were made with the GPR along each Transect Line. J = January 2010, O = October 2010, A = August 2011.

and any uncertainty, will affect estimated wave velocity, and estimated penetration depth. We therefore perform a time-depth calibration whenever possible and discuss what actual variability from this measured dielectric estimate may be. While dielectric of the subsurface is important in any radar wave study, we are primarily interested in documenting and measuring subsurface structure. The contributions of subsurface structure to the measured radargrams can still be characterized and compared from place to place with imperfect encapsulation of the subsurface dielectric. If we reasonably estimate the dielectric at our field site, then the results of apparent block detections per cubic meter may be compared with those obtained from a remote site at which the dielectric is also reasonably estimated.

3.1. Field GPR Methods

[21] All of our individual study sites at Meteor Crater are within the limits of the continuous ejecta blanket, ~200–450 m to the south of the rim. For purposes of this study, we classify our eight individual sites into three types of ejecta (detailed in following section). Many of the sites contain multiple GPR transect lines, along which multiple measurement runs are made (Table 1). Individual transects are (in most cases) measured with both 400 and 200 MHz antennas (Figure 2). Frequency-cut filters applied during data collection were nominally 100–800 MHz for the 400 MHz antenna and 50–600 MHz for the 200 MHz antenna. With each of the two antennas, transects are repeated at multiple depth ranges, typically of 30–80 ns and 60–160 ns two-way travel times, respectively. Returns are sampled and quantized into 512 or 1024 samples per scan trace, or column, by the GPR. GPR transects and visual counts of rocks in preexisting excavations into the ejecta are done within areas of contiguous similar geology, as close to each other as possible. GPR transects are slightly set back from these existing ground-truth pits because the vertical air-outcrop interface would produce returns if the transects were positioned along the very rim of the pits. Data collection in October 2010 and August 2011 involves a survey wheel to ensure precise 2 cm (occasionally 1 cm) spacing of subsurface scans. In January 2010, marks every few meters are entered manually in the field while pulling the radar in continuous scan mode. Postcollection distance normalization adjusts for sections where the radar was not being pulled at a constant rate.

[22] At most sites, measurement of a metal plate buried at a known depth (~30–50 cm) serves to estimate the local, subsurface radar wave propagation velocity and dielectric constant, using the relationships in equations 1 and 2. Dielectric values obtained in this way (~3.5–5.2) are consistent with the range of values obtained from ejecta materials (4.0–5.3) by *Grant and Schultz* [1994]. Independent, postcollection estimates of bulk subsurface dielectric values derived by fitting hyperbolas to reflectors in the radargrams typically yield values of ε (~4–8) similar to or higher than those determined in the field with the buried metal plate target. As the hyperbola-fitting sampled depths greater than possible with the metal plate, the larger dielectric values are likely the result of increasing soil moisture at depth. No indications of a sudden change in dielectric over the whole of a transect (e.g., significant geological horizon, water table) appear in the data. The possibility of higher dielectric at depth means that counts per meter of depth may be slightly underestimated at greater depths (e.g., the second or third meter below the surface). In calculations, we use the plate-derived values of ε, which are likely low by up to a factor of <2 (recall that most parameters scale by $\sqrt{\varepsilon}$) for depths ~1 m. Measurements of the dielectric are typically made in

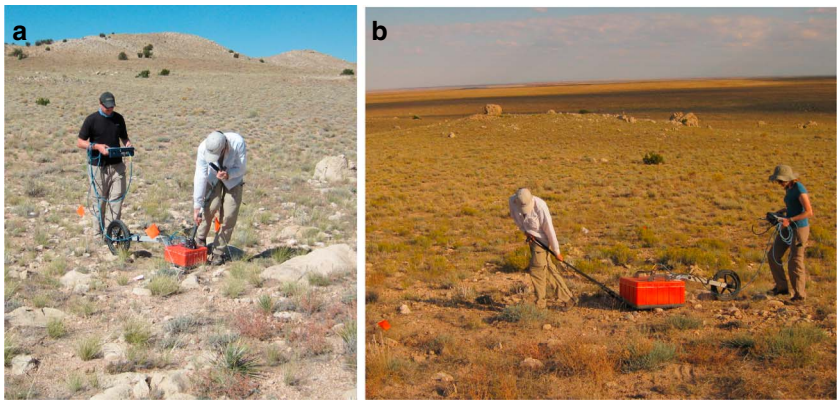

Figure 2. Ground penetrating radar (GPR0 field deployment, including orange antenna dragged directly on the ground, trailing odometry wheel, and hand-held SIR-3000 control unit. (a) 400 MHz antenna at Site 1, looking NNW toward the crater rim. (b) Site 2, 200 MHz antenna, looking SW toward low mound of Site 1.

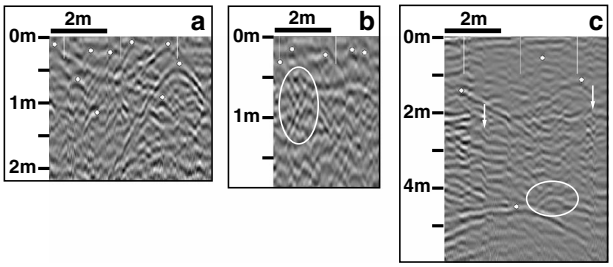

Figure 3. Examples of apparent block counts (white dots) and features which are not counted. (a) One particularly good, near-ideal hyperbola exists at right, while other counts are rounded apexes with at least one hyperbola-like tail. Features just left of and below good hyperbola are generally too small and/or pointed to include in counts. Site 2, 400 MHz. (b) Prominent upward-pointing "V" pattern throughout the mid and lower sections, which begins to resemble a crisscrossing "X" pattern when several adjacent "V"s interfere with each other (white circle). These and other sharp apexes are not counted. Site 2, 400 MHz. (c) Example of a rounded-apex form that is uncharacteristically narrow for its depth (white circle) and of two instances at which an abrupt vertical shift in a group of scans can be recognized up and down most of the height of the radargram (arrows). Site 2, 200 MHz.

only one transect per site; this value is then used for all transects within the site, as well as for any nearby sites of the same ejecta material if no measurement was made at that site. The dielectric is not assumed constant over different field seasons, i.e., dielectric measurements are only applied to transects taken in the same field season, primarily due to concerns with current local soil moisture content, which can significantly affect radar wave velocity. There had been some recent rain before the August 2011 field season. October 2010 was quite dry. During January 2010, there was patchy snow on the ground but any melt appeared to evaporate quickly. The upper several decimeters were dry to only very slightly moist in all field seasons.

3.2. GPR Data Processing

[23] Postcollection processing is done using GSSI's RADAN™7 software. The goal is to enhance returns by increasing contrast and sharpness of the data, while removing noise and background; absolute signal amplitude is not rigorously tracked in this study. A time-zero correction adjusts the vertical time scale to be relative to the surface. Persistent horizontal bands in the data are removed with a 201 or 401 column-wide moving boxcar filter. High-pass and low-pass filters are effective in sharpening the data in some profiles and have little effect in others. In general, there is little high frequency or speckle noise in the down-column direction above ~45–80 ns, depending on antenna and site (discussed further below). A moving-average filter three to five columns wide softens some of the abrupt offsets and distortions from one column to another (or between sets of columns). Many along-profile contrasts and discontinuities in amplitude, lateral continuity, and vertical penetration, likely caused by variable antenna-ground coupling due to the antenna bumping and tilting over the rough terrain, could not be removed. It is sometimes possible to follow returns through such an area with the eye; in a few cases, the disruption is bad enough that those columns of the profile are excluded from counting and the profile length. Manual and automatic exponential gains are applied so as to try to achieve a fairly uniform overall brightness and contrast over the whole depth and length of the radargram.

3.3. GPR Radargrams and Block Detections

[24] The inherently blocky nature of crater ejecta at our sites often leads the ejecta volume as a whole to appear highly scattering to radar waves, hence yielding cluttered radargrams (Figure 3) that make certain identification of individual blocks in the radargrams difficult. As stated above, we seek the GPR characteristic signature of a rock population that is known from visual counts. It is accepted that GPR counts are not going to equal the exact number of blocks in the subsurface, for reasons detailed below. Rather than expecting a one-to-one correlation of detections and exact block locations, we note that the radargram was produced from the entire existing block population and distribution and through the net interactions (single and multiple) of radar waves, and thus, that the counts of "apparent blocks" do reflect the actual radar signature of the block population. Determining whether the GPR counts yield values above or below the actual number of blocks, and by how much, is one of the goals of the study. The main focus of our study is comparing apparent detections with actual subsurface counts in order to link GPR results to geologic process. We do not explicitly investigate how the convolution of radar waves and reflections responds to and develops from a particular configuration of rocks to produce the individual corresponding features in a radargram. Significant prior work, using various simulation techniques, has investigated this latter topic with planetary considerations [e.g.,, *Soldovieri et al*., 2009; *Valerio et al*., 2012; *Leuschen et al*., 2003b; *Pettinelli et al*., 2007].

[25] Given the high concentration and dense packing of variously sized rocks around and below the radar wavelength, the classic hyperbola pattern produced by an isolated object in a contrasting, uniform matrix, as described above, is seldom ideally developed (Figure 3a). We here develop the criteria by which a GPR detection is counted as an apparent block in a radargram. In the instance of this study, it is generally more effective to count blocks in unmigrated data. Migration is a data-processing technique by which hyperbola tails are "collapsed" to the location of the source object; the return power in the tails is concentrated at the nose of the hyperbola, thus emphasizing point reflectors and interfaces and deemphasizing the detection effects inherent to the moving GPR. It is difficult to tell in migrated data which brighter points are due to buried blocks and which are likely products of the complexly cluttered subsurface and the disruptions caused by pulling the GPR over rough ground. In contrast, the presence of any hyperbola-like features in unmigrated data is used to advantage in counting blocks (Figure 3a).

[26] Many reflections off multiple objects often lead to a crisscrossing pattern of narrow, upward-pointing (i.e., upside-down), overlapping, interfering, sharp-tipped "V"s (Figure 3b). These are frequently traceable up to the very near surface (0–15 cm deep). The prevalence of these near-surface origins and the apparent persistence of the "V" tails

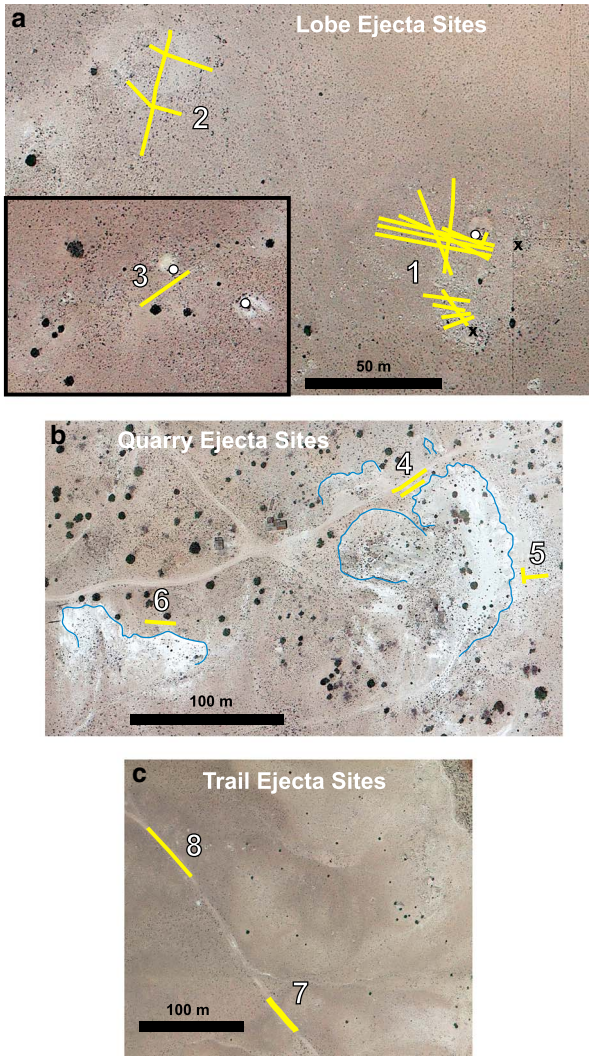

Figure 4. Study sites with individual GPR transect ground tracks (yellow) at each site (areas enlarged from boxes in Figure 1a). Small dark dots and larger blobs are shrubs and trees. (a) Lobe ejecta, Sites 1–3. White dots are preexisting pits with subsurface exposures; (b) Quarry ejecta, Sites 4–6. Blue lines are traces of quarry scarps; (c) Trail ejecta, Sites 7–8, along an abandoned jeep track.

to depth (actually an indication that the origin point is visible to the antenna while the antenna is some distance away) suggest that the GPR may be picking up blocks embedded in and just below the surface very effectively, relative to blocks at depth. In contrast to these "V"s, a rounded, convex-up arc resembling a hyperbola-like nose is considered a possible detection and is counted as such if at least one tail descends from it in a fashion that is nonparallel to any immediately adjacent upside-down "V" tails or other local patterns (Figure 3a). Any sharp, nonrounded apex is excluded. In effect, the type and extent of criteria for counting an apparent block are similar to what they would be in a sparse subsurface with a few well-defined objects: picking hyperbola-like forms out from the background signal. In this case, however, there is likely to be distortions or additional interference convolved with any hyperbolic form.

[27] Typical types of interference, noise, and artifacts are also excluded. With depth, the hyperbola associated with an object is expected to widen. Any rounded-apex forms at depth that are significantly narrower than hyperbola-like noses typical of shallower depths, within a given radargram, are excluded (Figure 3c). The vertical offset of a group of successive scan traces relative to neighbors or the rise and fall of a group of near-horizontal bands sometimes appears to create hyperbola-like forms. Due to the stacked nature and parallel behavior of such patterns, shifting abruptly up or down in the along-column direction, they can be linked to variability in the location and coupling of the antenna over nonuniform ground, and hence excluded (Figure 3c). Possible detections consisting of hyperbola forms that are directly below, and the same shape as, such forms above them are likely multiples of the upper return and are also excluded.

[28] All radargrams are adjusted to the same on-screen horizontal and vertical scale before counting, to maintain relative shape within all radargrams. The task of counting is accomplished within GSSI's RADAN™7 software and involves placing a single "pick" at the nose of the detection, thus recording its horizontal location and vertical time-depth below the surface (e.g., Figure 3a). These values are exported for each transect for analysis. While the depth below the surface of each detection can be easily gleaned by applying the local dielectric to the time-depth profile, the size of blocks cannot be easily determined with the GPR if they are too small to produce a significant flattening of their signature in the radargram. Given the resolution estimates in section 1.2, it is expected that the 400 MHz will register returns from blocks ~18 cm in diameter at 20 cm depth, 35–43 cm across and larger at ~1 m depth, and ~50–60 cm across at ~2 m depth. The 200 MHz should pick up returns from blocks a factor of $\sqrt{2}$ wider at the respective depths.

[29] Besides number and depth of block detections, the length and depth of the counting zone are needed to compute counts per m^2 or per m^3. The first and last meter of transects are excluded from counting and from transect total length, as are regions directly below the signal of the buried metal calibration plate. A maximum depth range, in ns, is determined individually for each transect by the point at which returns become indiscernible. All time ranges are converted to depths using the dielectric constant from the most applicable plate-calibration site, as described above. The upper 20 cm, for the 400 MHz antenna, or 40 cm, for the 200 MHz antenna, is also neglected in each transect, for several reasons. While there are apparently frequently many detections in this upper surface, as mentioned above, variation in the clarity of this upper zone between transects would have the potential to heavily skew results and comparisons among transects. This zone may also be difficult to separate from the dominant antenna direct wave and surface return, the latter of which also varies with surface roughness and degree of antenna-ground coupling. Finally, the ejecta surface is susceptible to deposition of fines amongst blocks and/or concentration of blocks in a surface lag due to vertical erosion; estimates of such erosion of Meteor crater ejecta are estimated to be, on average, < 1 m [*Grant and Schultz*, 1993]. For analysis of block counts with depth, results are binned by depth, nominally in 1 m increments down to 3 m. The shallowest

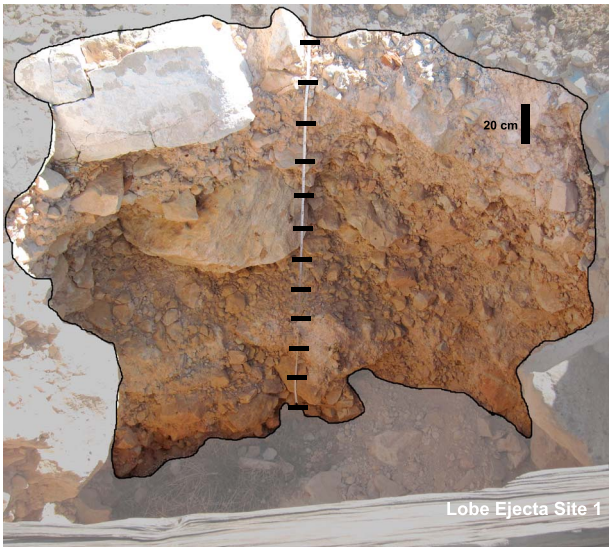

Figure 5. Preexisting outcrop exposure into the Lobe ejecta subsurface at Site 1 in a preexisting prospecting pit. Nongrayed portions are examples of areas within which blocks were counted and measured in the visual "ground-truth" block counts. Horizontal black bars represent 20 cm increments along tape measure.

zone begins at 20 or 40 cm, and the maximum depth for any transect is the actual observed maximum depth of penetration, not the nearest or next-greatest, whole number of meters.

3.4. Visual Methods

[30] The "ground-truth" visual rock counts take advantage of preexisting prospecting pits and quarries so as not to further disturb the intact ejecta environment. Exposure walls are digitally photographed in the field. A known, graduated length scale, such as a measuring tape, is included in the images to account for changing pixel scale over the field of view. These photos are then digitally mosaicked together, changes in the length scale are accounted for, and a section of the wall is delineated, before the blocks in that section are counted and measured in terms of long axis and depth. Using the area of the wall section, an areal density of blocks of a given size is calculated, which is then converted to an estimate of volume density (by raising the number of blocks per m^2 to the power of 3/2) for direct comparison to radar results.

4. Field Sites

[31] Our eight sites cover three areas of ejecta to the south of the crater, designated for purposes of this paper as the "Lobe," "Quarry," and "Trail" ejecta sites (Figure 1a and Figures 4a, 4b, and 4c, respectively). The dominant lithology of blocks observed at GPR site locations is consistent with the geologic map of Shoemaker (1960, Figure 1b), although blocks of all three lithologies are often present at the surface.

4.1. Lobe

[32] Sites 1–3 are spread over three low mounds of Lobe ejecta (Figure 4a and Table 1). At these sites, blocky lobes of ejecta are composed of mixed clasts from several cm up to ~1.5 m across. Views into the subsurface are afforded by small preexisting prospecting pits that had been dug near the crest of the ejecta lobes. In the subsurface, blocks are subangular to angular with a closely packed matrix of smaller clasts and finer grains (Figure 5). In the immediate near surface, the matrix is a loose, dry, silt-rich soil, likely reflecting incorporation of eolian fines [*Grant and Schultz*, 1993a and b]. Weathering has rounded the edges of Kaibab and friable Coconino blocks at the surface. Site 1 (Figures 6a and 6b) is on a low, isolated mound of ejecta ~450 m from the SE crater rim, dominated by blocks of Kaibab. Two nearby surface boulders are ~2.5 m across. The pit on this mound, roughly 2 × 2 m square and ~2.5 m deep, represents one of the most extensive views of the subsurface ejecta at Meteor Crater.

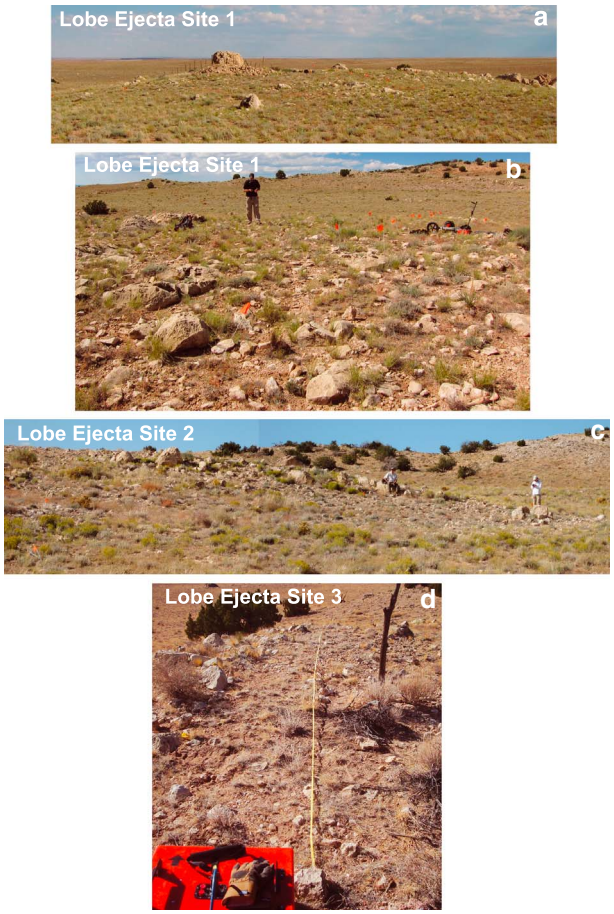

Figure 6. Photos of surfaces and context of Lobe ejecta sites. (a) Site 1, mound of ejecta. Preexisting pit in Figure 4 is located in front of large ~2.5 m ejecta block. Orange flags indicate two roughly perpendicular transect lines. (b) Site 1, surface rocks dominated by Kaibab. Preexisting pit is off image by clump of grass at right edge. Orange flags same as in Figure 6a. Ridge of ejecta of Site 2 visible between 400 MHz antenna GPR system and distant crater rim in upper right. Knob of ejecta of Site 3 visible at upper left. (c) Site 2, mound of ejecta primarily Kaibab with some Coconino at lower left. Standing person and scattered orange flags mark parts of three transects. (d) Site 3 surface at top of Kaibab-dominated ejecta ridge. Yellow tape runs along transect. Shallow preexisting pit is directly off image to right. Foreground, 200 MHz antenna.

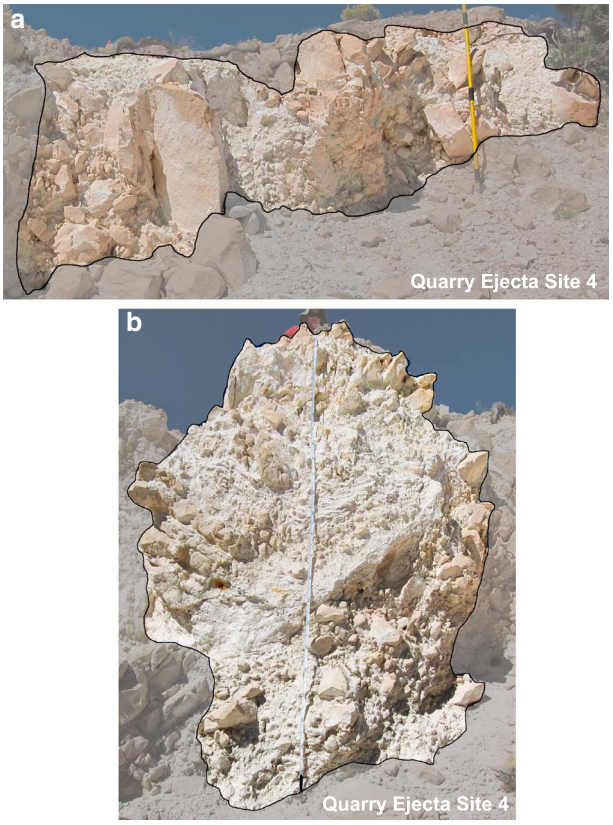

Figure 7. Preexisting outcrop exposures into the Quarry ejecta subsurface in the north quarry wall below Site 4. (a–b) Two sections of wall exposing fractured and pulverized Coconino. Nongrayed portions are examples of areas within which blocks were counted and measured in the visual "ground-truth" block counts. Yellow staff in Figure 7a is ~1.8 m; tape in Figure 7b is ~2.4 m.

Site 2 (Figure 6c) is located on the crater-distal side of a low ridge of ejecta that runs discontinuously E to W, ~400 m from the S/SE crater rim, facing Site 1. The surface hosts both Kaibab and Coconino blocks. A large fairly intact chunk of Coconino, with undeformed internal bedding, is present at the south end of the site. No subsurface pit was available at Site 2. Due to proximity, it is here linked with Site 1 for purposes of dielectric determination and ground-truth pit block counts. Site 3 (Figure 6d) is on the discontinuous ridge of Site 2, further along to the W, and is dominated by Kaibab blocks. A shallow preexisting pit also ~2 × 2 m square but only up to ~0.5 m deep is located on the ridge top.

4.2. Quarry

[33] Sites 4–6 are located within the Quarry ejecta (Figure 4b and Table 1), composed predominantly of overturned Coconino that has been heavily fractured and in some areas has had its constituent pure, bright silica sand grains pulverized into a floury texture. Good 2–3 m high exposures of this material are laterally extensive along the boundaries of a defunct silica quarry ~200–300 m from the S/SW crater rim. On an outcrop scale, pulverized areas are interspersed with concentrations of fracture-permeated, more coherent sandstone (Figures 7 and 8). While the fractures define individual blocks on the scale of 10s of cms, these blocks often have maintained their position relative to their neighbors from which they were fractured apart (Figure 8a). Internal bedding is sometimes still visible within blocks (Figures 8b and 8c). The boundaries between coherent blocks and pulverized material range from sharp and distinct, to gradual and diffuse (Figures 7b and 8d). Overall, the deposit appears as a uniform-composition material that has been physically affected to differing degrees by emplacement. The immediate surface of the pulverized outcrops is littered with loose blocks of Coconino (typically tabular and <30 cm) which may have been disturbed by human activity. Site 4 is on the crater-ward rim of the eastern quarry pit (Figure 9a). Site 5 is on the eastern rim of the eastern quarry pit (Figure 9b) where the surface hosts small clasts of all three rock types, mostly scattered across, but occasionally embedded in, the fine-grained silica-sand surface matrix. Site 6 is on the crater-ward rim of the western quarry pit. It crosses a slight depression in the surface, which,

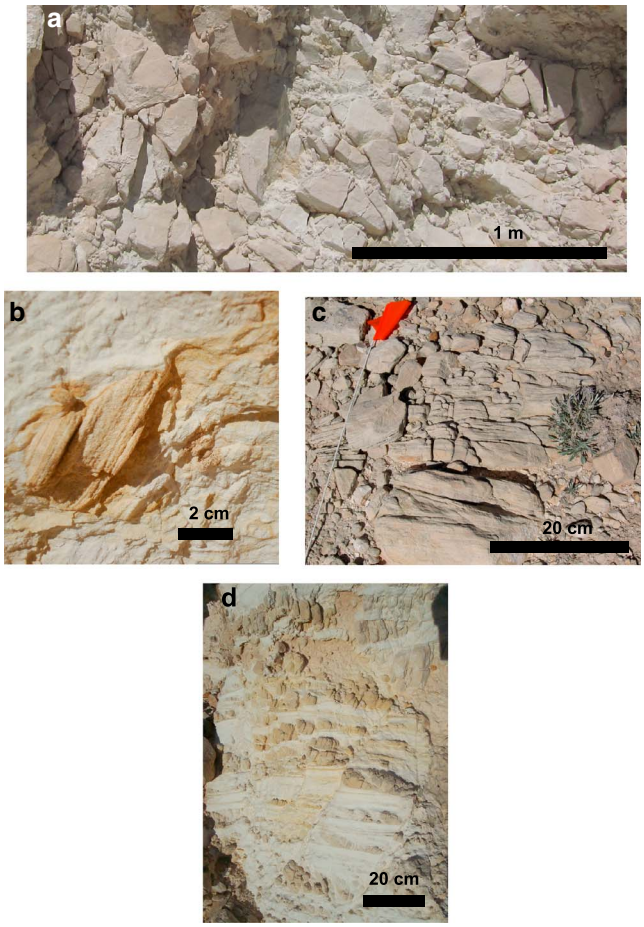

Figure 8. Details of Quarry ejecta subsurface. (a) Example of Coconino sandstone blocks within quarry walls that have been heavily fractured yet minimally displaced from their fragment complement(s). (b) Small-scale example of preserved bedding within fragments of Coconino in quarry wall. (c) Fractured yet minimally displaced block of Coconino exposed at surface, with excellent preserved parallel- and cross-bedding. (d) Example of small-scale inhomogeneity of physical alteration within overturned Coconino, ranging from pulverized zones to fractured blocks, also apparent in Figure 7b.

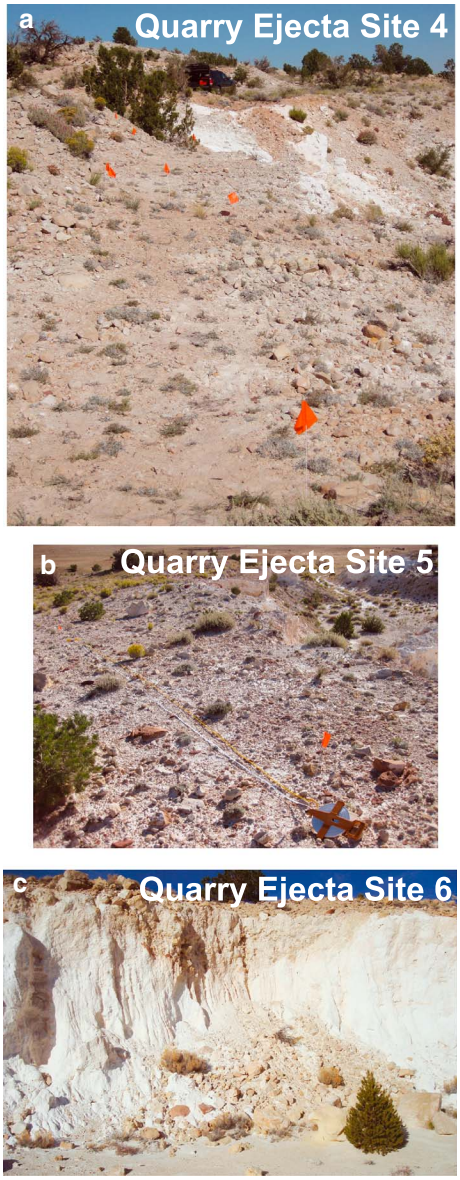

Figure 9. Photos of surfaces and context of Quarry ejecta sites. (a) Site 4, thin disturbed Coconino rubble above north quarry wall. Edge of wall scarp runs diagonally across upper right quadrant of image. Orange flags mark transect. (b) Site 5, thin disturbed mixed-lithology rubble above east quarry wall. Edge of wall scarp runs along right of image. Edge of wall scarp runs diagonally across upper right quadrant of image. Orange flags and tape mark transect. (c) Site 6, located above and along northwest quarry wall (transect not visible, over and behind scarp lip), as seen from quarry floor. Bright wall material is fractured and pulverized Coconino, but note apparent mixed-lithology material filling depression in Coconino wall material and concentrated directly below at foot of scarp.

seen in cross section in the quarry wall, appears to reflect a gouge in the upper surface of the fractured and pulverized ejecta that is filled with blocks of mixed lithologies and matrix (Figure 9c).

4.3. Trail

[34] The Trail ejecta (Figure 4c and Table 1) is cut by a jeep trail which provides a convenient, relatively smooth surface over which to drag the GPR antennas (Figure 10), in contrast to the blocky, and consequently bumpy, surfaces at the other sites. The less rugged surface of the trail is tested to see how it would affect returned data in terms of possible clutter and disruption. The more subdued ejecta lobes here are visibly eroded, with more soil development and grass cover, as well as more rounded surface blocks, primarily Kaibab. The primary views to the subsurface are two shallow stream cuts, revealing blocks of all three lithologies, both loose and firmly embedded in the substrate. Upslope are rilles cut into the steeper ejecta rim. This ejecta has, at least at the surface, likely been affected by alluvial and colluvial transport and/or burial [*Grant and Schultz*, 1993]. Sites 7 and 8 are along the soil- and gravel-covered jeep trail running roughly NW-SE, ~ 300 m from the S/SW crater rim. The trail gently cuts through low lobes and over shallow swales and is adjacent to one of the field sites of *Grant and Schultz* [1993].

5. Results

5.1. Visual Ground-Truth Block Counts

[35] The number, size, and depth of blocks in existing exposures of the subsurface are measured from photos as "ground truth" for the subsurface rock size-frequency distribution. At Site 1, exposures in the four walls of the preexisting ~2.5 m deep pit are counted to characterize the block population in Lobe ejecta (Figures 4 and 11a). The same is done at Site 4 for five sections of the ~2.5 m high northern wall of the defunct quarry to characterize the bock population in the Quarry ejecta (Figures 8 and 11b). Counts at both sites fall off steeply with increasing block diameter, although there is variation in the rate at each individual exposure. There are few blocks larger than ~50 cm at either site and the maximum size is 108 cm in the pit and 125 cm at the quarry. The limited size of subsurface exposures over which blocks are counted limits not only the number of large blocks likely to be counted, but the largest size of block as well. Individual exposure counts are summed and divided by total exposure area to get an average count per m^2 at each site.

Figure 10. Photo of surface and context of Trail ejecta. Placement of transect along one of the tracks provided a smooth dragging surface for antennae. Trail crosses low lobes with higher surface ejecta-block concentration (midground) as well as shallow swales (foreground, background).

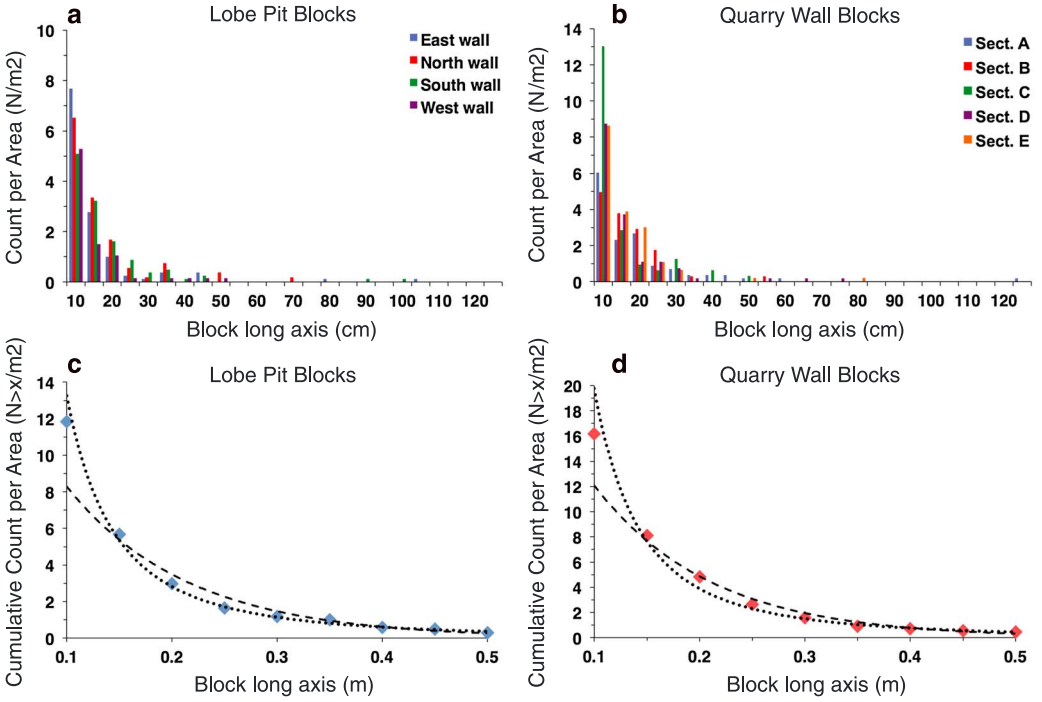

Figure 11. Visual "ground-truth" block-count results. (a, b) Plots of size-frequency block counts per m^2 for each individual section within the Lobe ejecta pit and the Quarry ejecta walls. Plotted in 5 cm bins against block long axis. (c, d) Plots of total (sum of individual sections) cumulative size-frequency block counts per m^2 for the Lobe ejecta pit and the Quarry ejecta walls. Results can be fit reasonably well with either power (equation 5) or exponential (equation 6) curves; power fits are slightly better over this size range. Diamonds: measured visual counts; dotted line: power fit; dashed line: exponential fit. Curve fits for Lobe ejecta have $a = 0.077$, $b = 2.23$, $R_{pwr} = 0.99$ (equation 5) and $k = 19.7$, $q = 8.66$, $R_{exp} = 0.97$ (equation 6). Curve fits for Quarry ejecta have $a = 0.088$, $b = -2.35$, $R_{pwr} = 0.99$ (equation 5) and $k = 30.1$, $q = 9.11$, $R_{exp} = 0.97$ (equation 6).

These data are expressed in terms of the cumulative number of blocks above a given diameter per square meter, $N(D)$, plotted against bins of diameter, D, in meters (Figures 11c and 11d). Due to the paucity of large blocks in our sample area, we only use those size bins of 50 cm (blocks with max diameter of 55 cm) and smaller in fitting a function to describe data trends. These data can be described very well with either a power or an exponential least squares fit, represented, respectively, by equations in the following form:

$$N(D) = aD^{-b} \tag{5}$$

$$N(D) = ke^{-qD} \tag{6}$$

[36] Power fits yield exponents, b, of 2.23 for rocks at the Pit and of 2.35 for rocks at the Quarry, while exponential fits yield exponent coefficients, q, of 8.66 and 9.11, respectively. Populations of rocks produced by explosion craters, terrestrial and lunar impact craters, and martian surface processes are found to be well described by power law distributions, thought to be a result of the degree of fragmentation experienced [*Melosh*, 1989; *Moore and Keller*, 1990, 1991]. However, rock populations on terrestrial and martian landscapes affected by a wide range of geologic processes have also been found to well approximate exponential functions, explained by theories of fracturing based on pervasive material flaws and due to transport processes [*Golombek and Rapp*, 1997, and references therein]. It is important to note that the Meteor Crater counts (e.g., Figure 11) are for the subsurface whereas many published counts in the planetary literature are for areas of the surface, at which different postemplacement processes may have affected the population (discussed further below).

5.2. GPR Block Counts

[37] Typical maximum penetration depths with the GPR are 50 ns two-way travel time (~3.5 m) in the Pit ejecta, 65 ns (~5 m) in the Quarry ejecta, and 40 ns (~3 m) in the Trail ejecta with the 400 MHz antenna, and 70 ns (~4.5 m) in the Pit ejecta, 80 ns (~6 m) in the Quarry ejecta, and 60 ns (~4.5 m) in the Trail ejecta with the 200 MHz antenna. Greater penetration in the Quarry material is likely due to the pure, well-drained silica sand and large clusters of fractured blocks of the same composition that have been minimally displaced from their complement fragments, while lower penetration at the Trail sites is likely due to the presence of more matrix, weathered soil, and possibly damper ground at depth, given their location downslope from eroded ejecta ravines.

[38] As discussed in section 3, the cluttered nature of many radargrams produced in response to a cluttered subsurface precludes that every apparent block detection in GPR data will directly represent an actual block in the subsurface, nor

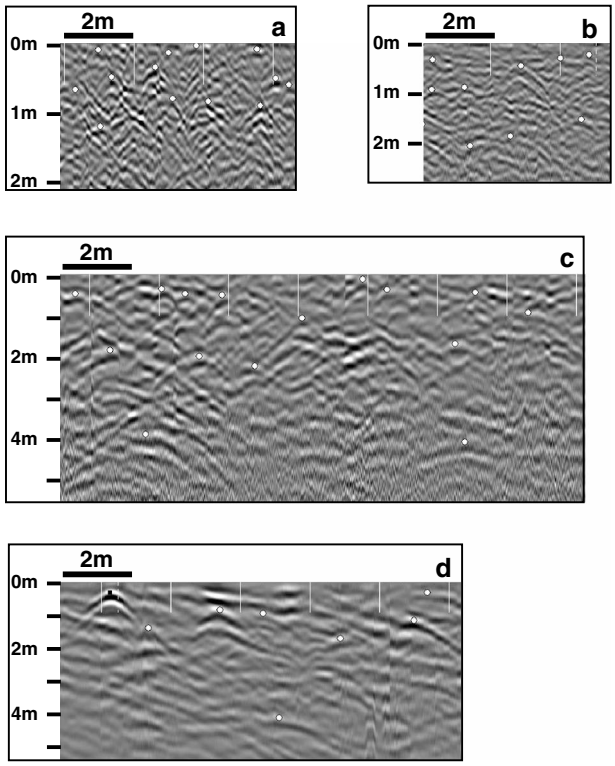

Figure 12. GPR radargrams with apparent block counts (white dots). (a) Site 1, 400 MHz; (b) Site 1, 400 MHz; (c) Site 1, 200 MHz. High-frequency noise visible at depth; (d) Site 4, 200 MHz. Black square in upper left denotes metal plate buried for time-depth calibration, done for each site according to local dielectric as described in text.

will every actual subsurface block be counted as a detection. By using the visual block counts in ejecta exposures as ground truth for the real block population, the relation of actual to GPR-derived block counts can be determined. Documentation of the resulting bias toward over-counting or under-counting relative to the actual population will yield a scaling factor relating the GPR counting metric to actual block population.

[39] The number and layout of GPR transects and their division amongst the eight sites and three ejecta types are summarized in Table 1 and Figure 4. Radargram count results are broken down by ejecta type in which they are located, antenna used during collection, and depth zone within the radargram. Figure 12 illustrates typical radargram examples for both the 400 MHz and 200 MHz antennas from Lobe and Quarry sites. Lobe 400 MHz radargrams are typically the most crowded, while the 200 MHz tends to smooth over much of this, leading to fewer detections but perhaps a clearer picture of the strongest reflectors (e.g., Figure 12d). Counts for each individual transect are shown in Figure 13a–13f, in which each of the six plots contains results for a different combination of the three ejecta types and two antennas. Table 2 summarizes these ejecta-type – antenna groups by average, standard deviation, and range. The values reported here, unless otherwise indicated, are radargram block counts per m^3, having been normalized to the volume of the subsurface sampled along the given transect and depth zone, as described above. The greatest number of GPR transects was taken in the Lobe ejecta, especially at Site 1, at which the large ground-truth pit provides the best opportunity for visual block counts. With the 400 MHz antenna (Figure 13a and Table 2), the average transect count is 1.6 m^{-3} (standard deviation, SD, 26%) in the upper 0.2 to 1 m of the subsurface and 0.3 m^{-3} (SD 38%) within the second meter of the subsurface (from 1 to 2 m deep). Counts in the Quarry ejecta (Figure 13c and Table 2) are similar (1.4 m^{-3} in the upper depth zone, SD = 26%, and 0.4 m^{-3} in the second meter, SD = 58%), whereas counts in the Trail ejecta (Figure 13e and Table 2) are lower and consistently exhibit the least transect-to-transect variability of any ejecta type (1.1 m^{-3} in the upper depth zone, SD = 15%, and 0.3 m^{-3} in the second meter, SD = 36%). Corresponding counts for the 200 MHz data (Figures 13b, 13d, and 13f) can be read from Table 2.

[40] In all ejecta-type – antenna groups, all transects but two (Site 1, 200 MHz, Transects #6 and #7, Figure 13b) have counts that are higher in the uppermost depth zone than in the 1–2 m zone. Counts below 2 m are infrequent and vary more erratically from transect to transect than those at shallower depths. Data points for the 2–3 m depth zone are included in Figure 13 for thoroughness but are minimally discussed due to sparse data. Counts from 1 to 2 m deep are usually similar to or higher than the 2–3 m counts, but are more regular and consistent between transects in an ejecta-type – antenna group.

[41] Within the upper-most meter, detections with the 200 MHz antenna are always lower than those with the 400 MHz antenna for each transect in the same ejecta-type – depth-zone group. In the second meter of depth, this relationship between antenna types is less pronounced, with counts in the second meter of Trail ejecta being very similar in the 200 MHz and 400 MHz data. Indeed, a pervasive characteristic of all ejecta types (for the upper meter anyways) is that the range of 400 MHz counts is exclusive of the range of 200 MHz counts. Counts at the Lobe and Quarry ejecta are similar to each other within each respective antenna-depth zone, in terms of both average and range. In the Trail ejecta, counts are lower than in the Lobe or Quarry ejecta with the 400 MHz antenna, but quite similar to the other ejecta types in the 200 MHz data. Counts in the Trail ejecta also consistently exhibit the least transect-to-transect variability of any ejecta type, reflected in significantly lower standard deviations.

6. Discussion

[42] Size frequency distributions of rocks in populations created by different geological processes, yet that in some way involve fragmentation, have been found in numerous studies to follow power law or exponential distributions [e.g., *Melosh*, 1989; *Moore and Keller*, 1990, 1991; *Golombek and Rapp*, 1997]. The visually counted cumulative block populations in the Lobe and Quarry subsurface ejecta have similar power law exponents, 2.23 and 2.35. This distribution is within the range that may be expected from previous observations of fragmented rocks, produced by both natural processes and experiments [*Turcotte*, 1992, and refs therein]: populations with a power law exponent of 2.1 to 2.9 include those produced by fragmentation of igneous rocks, coal, and ice, by nuclear and chemical explosions, by laboratory high-velocity impacts, by the cumulative processes that created and modified asteroid populations, and by fracturing within

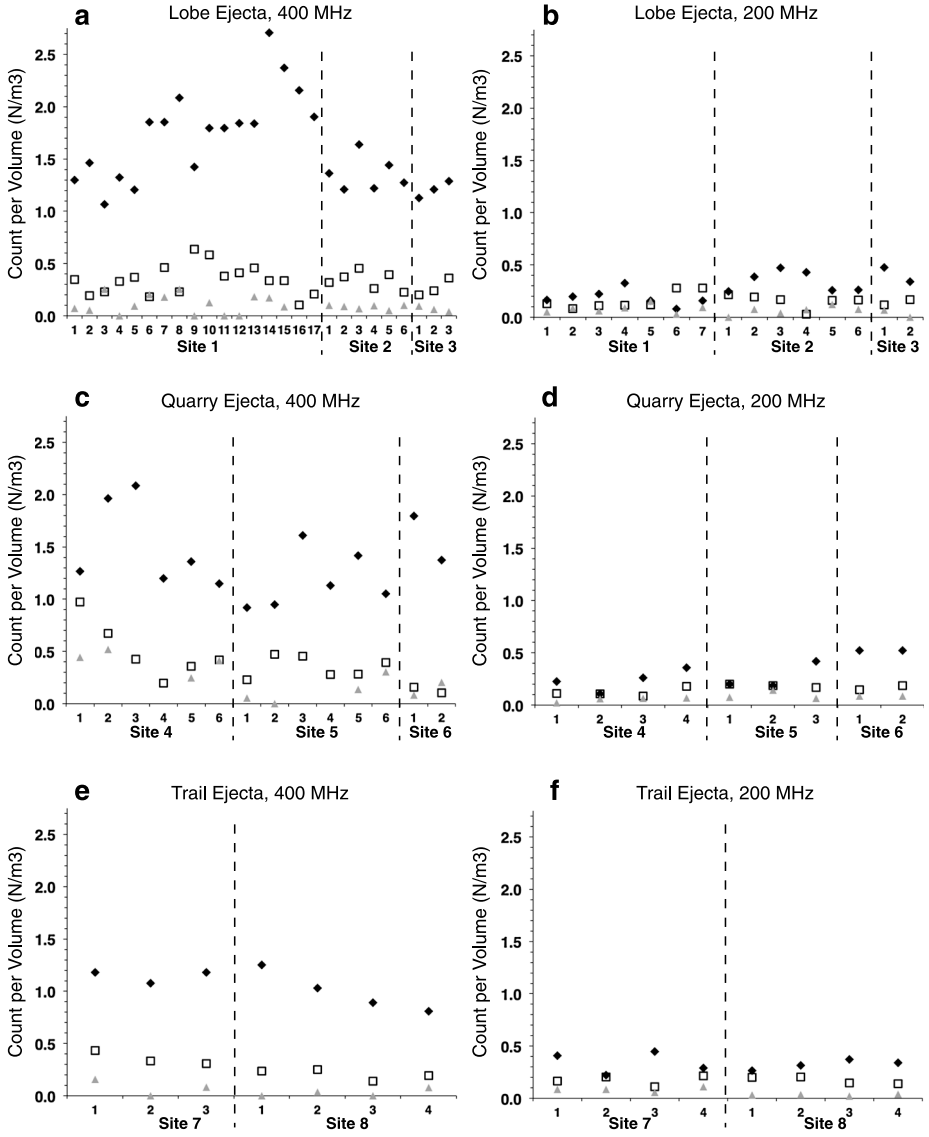

Figure 13. GPR radargram block-count results from individual radargram transects. GPR counts are by their nature cumulative of all sizes. (a) Lobe ejecta results from Sites 1–3 with the 400 MHz antenna and (b) 200 MHz antenna; (c) Quarry ejecta results from Sites 4–6 with the 400 MHz antenna and (d) 200 MHz antenna; (e) Trail ejecta results from Sites 7–8 with the 400 MHz antenna and (f) 200 MHZ antenna. Horizontal axis labels indicate individual transect run number within the given site (400 MHz and 200 MHz numbered independently); site data demarcated by dashed lines. Vertical axis values are per m^3 within the given depth zone. Black diamonds: counts from depths of 0.2 m (0.4 m for 200 MHz) to 1 m; hollow squares: counts from depths of 1 m to 2 m; grey triangles: counts from depths of 2 m to 3 m. Averages and standard deviations are given for each data series in Table 2.

fault zones (fault gouge). The applicable scale range for power law relationships is often limited by the physical nature of the material itself, such as the scale of the largest initial block radius or layer thickness (prior to onset of the fragmentation process), and the scale of the heterogeneities along which the fracturing may occur, e.g., grain or crystal size [*Turcotte*, 1992].

[43] Surface observations of ejecta from experimental, terrestrial, and lunar craters typically yield power law distributions with exponents (b) of 2.4 to 2.7 (converted to length from mass; [*Melosh*, 1989]). These values are generally more indicative of multiple fragmentation than single fragmentation, for which b ~1.2–1.8 (Melosh). Surface ejecta at Meteor Crater has previously been reported to follow a power law size distribution [*Shoemaker and Kieffer*, 1974]. The largest block within impact ejecta is also expected to scale with the crater size [*Gault et al*., 1963; *Bart and Melosh*, 2007], an example of the initial-size limitation mentioned above. Our subsurface measurements of b of 2.23 and 2.35 are slightly below the above range reported for impact craters, yet clearly indicate the dominance of multiple over single fragmentation. These values are similar enough to impart confidence that the ejecta population is reasonably accurately captured by our observations.

Table 2. GPR Block-Count Summary Statistics[c]

Ejecta Type	Antenna	Depth Zone[a]	Average[b]	Std. Dev.[b]	SD%	Range[b]
Lobe	400 MHz	0.2 – 1	1.6	0.4	26%	1.0 – 2.7
		1 – 2	0.3	0.1	38%	0.1 – 0.6
	200 MHz	0.4 – 1	0.3	0.1	44%	0.1 – 0.5
		1 – 2	0.2	0.07	43%	0.0 – 0.3
Quarry	400 MHz	0.2 – 1	1.4	0.4	26%	0.9 – 2.1
		1 – 2	0.4	0.2	58%	0.2 – 1.0
	200 MHz	0.4 – 1	0.3	0.15	48%	0.2 – 1.0
		1 – 2	0.15	0.04	27%	0.1 – 0.3
Trail	400 MHz	0.2 – 1	1.1	0.2	15%	0.8 – 1.3
		1 – 2	0.3	0.1	36%	0.2 – 0.5
	200 MHz	0.4 – 1	0.3	0.07	22%	0.2 – 0.5
		1 – 2	0.2	0.04	22%	0.1 – 0.3

[a]Values in m.
[b]Values in count per m^3.
[c]Each row corresponds to an ejecta type – antenna – depth zone data group plotted in Figure 10.

[44] Since the early days of robotic exploration, such power laws have been fit to and used to describe surface rock populations on the Moon [e.g., *Shoemaker and Morris*, 1969] and Mars [e.g., *Binder et al.*, 1977]. Rock counts of the surrounding area from Viking Lander 1 & 2 data suggest $b = 2.66$ for block sizes > 0.1 m [*Moore and Keller*, 1990, 1991]. However, *Golombek and Rapp* [1997] show that, while this power fit (in the form of equation 5) does well for sizes ~0.1–0.2 m up to ~0.5–0.8 m, sizes above and below, over a greater total range, are better fit by an exponential function in the form of equation 6. According to the theory that omnipresent, preexisting flaws, or cracks, inherent within a material (e.g., crystal or grain boundaries, voids, micro fractures) control fragmentation, the likelihood that a flaw exists that is weak enough to cause failure in a particle of a given size decreases with the size of the particle, leading to the exponential size distribution of resulting fragments [*Griffith*, 1921; *Gilvary*, 1961; *Gilvary and Bergstrom*, 1961; *Brace*, 1960; *Inglis*, 1913; *Weibull*, 1939; *Steacy and Sammis*, 1992]. Numerous terrestrial surface results [*Golombek and Rapp*, 1997] and additional Mars surface results from Pathfinder Lander [*Golombek et al.*, 2003], MER Spirit Rover [*Golombek et al.*, 2006; *Grant et al.*, 2006], and the Phoenix Lander [*Golombek et al.*, 2012] also reflect the tendency for populations to be reasonably described by a power law over some subrange within or overlapping 0.1 to 1.0 m, but to be generally better described by an exponential fit over the entire range of these surface counts (Figure 14). Orbital size-frequency counts of surface rocks using HiRISE data confirm that populations from ~1 m to several meters in size closely follow an exponential distribution at Viking Lander 1 & 2 sites, the final four proposed landing sites for MSL Opportunity, the Phoenix Landing site, and the northern plains of Mars in general [*Golombek et al.*, 2008, 2012; *Heet et al.*, 2009]. The range of block sizes over which we fit our data is determined by the range in which block counts are most robust: 0.1 – 0.5 m. That both power and exponential expressions fit our data well is consistent with all of the above findings because of the overlap of this robust-count range with the submeter range discussed above. As the power law fits our data slightly better (both visually and from $R_{pwr} = 0.99$ vs. $R_{exp} = 0.97$) over this range, we will use it when interpolating within this range.

[45] Comparing variations in size-frequency distribution curves for different sites and populations is useful because they reflect the net effects of all geological processes that have fragmented and otherwise operated on the population (e.g., Figure 14). The lesser falloff of block frequency at increasing size in our subsurface measurements compared with the multiple-fragmentation exponents or exponential fits found by other studies, above, may be due to better preservation of large blocks in the subsurface than in surface environments. In the case of Meteor Crater, our counts represent a subsurface ejecta that is very fresh, both in absolute age and in terms of weathering and transport, being largely covered and stationary for the ~50 K years since emplacement [*Nishiizumi et al.*, 1991]. At the surface, over time, further weathering and erosion may reduce the size of the larger blocks, favoring exponential distributions for exposed surface populations, including those listed for Mars, above. In contrast, subsurface fault gouge, fresh

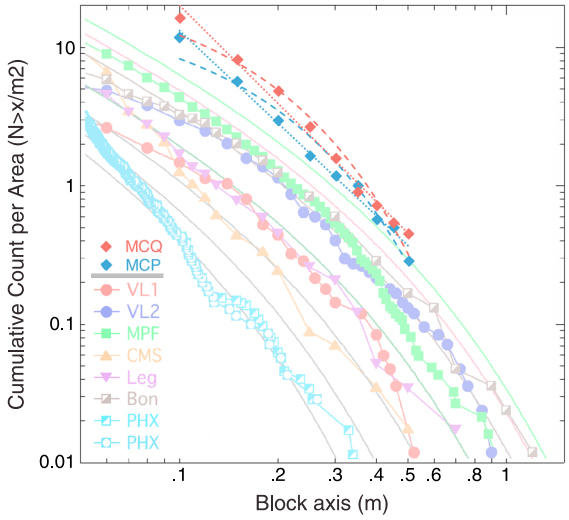

Figure 14. Visual block counts (cumulative counts per m^2) from the subsurface at Meteor Crater (MCP: Lobe ejecta pit; MCQ: Quarry ejecta wall; diamonds: measured visual counts; dotted line: power fit; dashed line: exponential fit) compared with surface counts from Mars landers at their respective landing sites (faded colors, from *Golombek et al.*, 2012, with data from: VL1 & 2: Viking Lander 1 & 2 [*Moore and Keller*, 1990, 1991]; MPF: Pathfinder [*Golombek et al.*, 2003]; CMS, Leg, Bon: Spirit sites Mission Success, Legacy, and Bonneville (*Golombek et al.*, 2006); PHX: Phoenix [*Heet et al.*, 2009]).

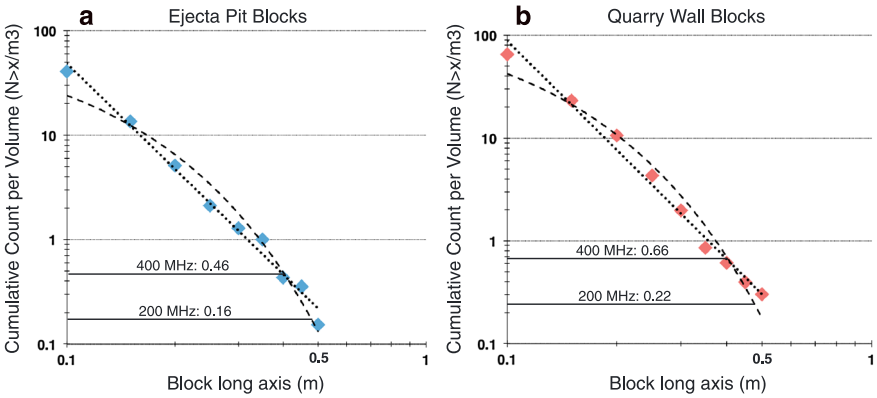

Figure 15. Visual "ground-truth" block count results from Figure 11 displayed as equivalent cumulative size-frequency block counts per m^3 for (a) the Lobe ejecta pit and (b) the Quarry ejecta wall. Diamonds: measured visual counts; dotted line: power fit; dashed line: exponential fit. Interpolating from this plot allows estimation of how many blocks are present at a given size. Annotations show estimations for the approximated minimum resolutions of the 400 MHz and 200 MHz antennas. See also Table 3.

laboratory and experimental crushing and cratering products, and atmosphere-less lunar crater ejecta, cited as examples of power law distributions above [*Turcotte*, 1992; *Melosh*, 1989], may share with subsurface Meteor Crater ejecta the characteristic of being relatively unaltered by secondary processes and maintain relatively more larger blocks. More definite interpretations and extrapolations of the behavior of larger block sizes are necessarily limited because, although blocks up to ~1.2 m are present in our observations, the limited size range over which our data are fit is well characterized by both power law and exponential distributions, as is typical for other populations [e.g., *Golombek and Rapp*, 1997]. Our subsurface block size-frequency distributions are dependent upon the isolated, spot sampling afforded by preexisting exposures into the subsurface. In comparisons with craters elsewhere or in the literature, it should be noted that all of these locations are ~200–450 m from the crater rim (~0.2–0.5 crater diameters). In comparing with whole-ejecta blanket counts or counts at other distances, consideration should be given to how block size may vary radially from the crater [e.g., *Bart and Melosh*, 2010].

[46] In the GPR data, the detection of more apparent blocks in the 400 MHz data than in the 200 MHz data (within the upper 2 m) may be expected for two reasons. First, the shorter-wavelength antenna detects smaller blocks as well as the larger blocks to which the longer-wavelength 200 MHz is limited. Second, there are many more of these smaller blocks than there are larger blocks, given the power law size distribution. While the 200 MHz antenna does not reveal more blocks than the 400 MHz at depths between 1 and 3 m, it allows more useful data to be collected to greater depths, reaching up to 4 or 5 m. These depths are beyond the observed < 3 m range of useful data collected with the 400 MHz antenna. Thus, the 200 MHz adds information not available solely from the 400 MHz, showing that occasional large blocks do exist at depth. There is a severe drop off in block counts with depth in the radargrams, even though the ejecta in which they were collected shows no trend in decreasing number of blocks with depth in visual data. This disparity suggests that the ability of the radar waves to propagate down and back coherently enough to "see" a block at depth is impeded not only by dielectric losses to the medium through which they are traveling, but also due to complex, multiple reflections and scattering of the radar signal by the observed dense structural packing of blocks in the ejecta. In such an environment, where postreflection waves may be disrupted before returning to the transceiver, larger objects have a better chance of returning a coherent radargram feature. These results augment suggestions that GPR waves in planetary volcanic terrain may suffer composition-dependent attenuation [*Paillou et al.*, 2001; *Heggy et al.*, 2001; *Stillman and Olhoeft*, 2008; *Williams and Greeley*, 2004; *Pettinelli et al.*, 2006] by demonstrating that penetration may be limited at least as severely by near surfaces crowded with structural scatterers. Similar conclusions have been drawn based on poor radar returns at depth recorded from beneath impact-crater breccia at Haughton impact crater [*Unrau et al.*, 2010], due to fractured bedrock at small impact craters in the Egyptian desert [*Heggy and Paillou*, 2006], and in the heterogeneously welded Bishop Tuff [*Grimm et al.*, 2006].

[47] Conversion of the cumulative visual areal block counts to an equivalent cumulative volumetric or density value allows the visual ground-truth population and the

Table 3. Comparison of GPR Average Results to the Value Interpolated From the Power Fit to the Cumulative Visual Counts (per Unit Volume) Corresponding to a Diameter Equal to the Estimated GPR Resolution (400 MHz: ~40 cm, 200 MHz: ~55 cm, Both at 1 m Depth)[c]

Ejecta Type	GPR Antenna	GPR Depth Zone[a]	GPR Count[b]	Visual Count[b]
Lobe	400 MHz	0.2 – 1	1.6	0.46
		1 – 2	0.33	0.46
	200 MHz	0.4 – 1	0.28	0.16
		1 – 2	0.16	0.16
Quarry	400 MHz	0.2 – 1	1.4	0.66
		1 – 2	0.39	0.66
	200 MHz	0.4 – 1	0.31	0.22
		1 – 2	0.15	0.22

[a]Values in m.
[b]Values in (cumulative) count per m^3.
[c]Interpolation at this size allows comparison of visual and GPR counts at the size the GPR is likely "seeing."

GPR apparent population to be linked directly. Assuming that the GPR is seeing blocks of a minimum size equivalent to its lateral resolution (~40 cm for the 400 MHz antenna and ~55 cm for the 200 MHz antenna, at depths of ~1 m), we can compare the GPR count with the visual count at that size, in order to determine the relationship of the GPR counts to the ground-truth counts. To determine the true abundance of rocks with a given minimum size, we fit the cumulative visual counts per unit volume with a power law, which in turn is used interpolate to the GPR's "resolution size" (Figures 15a and 15b). The following comparisons are also displayed in Table 3. For the Lobe ejecta, our visual block counts predict that there should be 0.46 blocks $m^{-3} \geq$ ~40 cm across; GPR counts yield 1.6 m^{-3} in the upper depth zone and 0.33 m^{-3} in the second meter measured with the 400 MHz antenna. For the 200 MHz antenna, visual counts suggest that there should be 0.16 $m^{-3} \geq$ ~55 cm across, and GPR counts yield 0.28 m^{-3} and 0.16 m^{-3} in the upper two depth zones, respectively. For the Quarry ejecta, visual block counts predict that there should be 0.66 blocks $m^{-3} \geq$ ~40 cm across; GPR counts yield 1.4 m^{-3} in the upper depth zone and 0.39 m^{-3} in the second meter measured with the 400 MHz antenna. For the 200 MHz antenna, visual counts suggest that there should be 0.22 $m^{-3} \geq$ ~55 cm across, and GPR counts yield 0.31 m^{-3} and 0.15 m^{-3} in the upper two depth zones, respectively.

[48] In both ejecta types, the 400 MHz GPR measurements of blocks in each of the upper two depth zones bracket the visual count at block sizes appropriate for 400 MHz resolution at 1 m depth (≥ ~40 cm). GPR detections, 200 MHz, of blocks in the upper two depth zones of both ejecta types also bracket the visual count at block sizes appropriate for 200 MHz resolution at 1 m depth (≥ ~55 cm), although the visual counts are at the low end of this bracket in the Lobe ejecta. Thus, according to both GPR frequencies used, the true population in the upper depth zone is overestimated by the GPR counts and that the population in the second meter of the subsurface is underestimated. Specifically, overestimations are 3.5x (400 MHz) and 1.8x (200 MHz) in the Lobe ejecta and 2.1x (400 MHz) and 1.4x (200 MHz) in the Quarry ejecta. Within the 400 MHz data, GPR detections are higher relative to their respective visual counts in the Lobe ejecta than are the GPR counts relative to their respective visual counts in the Quarry ejecta. In other words, because the ratio of upper depth-zone GPR counts to visual counts is higher in the Lobe ejecta (~3.5) than in the Quarry ejecta (~2.1), the overestimation of GPR counts is more in the Lobe ejecta. This relation also holds in the 200 MHz data (overestimation of ~1.8 in Lobe and ~1.4 in Quarry). GPR detections at both frequencies underestimate (by a factor of 0.6–1.0, 1 being in agreement with) the blocks in the second meter, yet again GPR detections relative to visual counts are higher in the Lobe ejecta (0.7 and 1.0, with 400 and 200 MHz, respectively) than in the Quarry ejecta (0.6 and 0.8), i.e.,, the GPR underestimates are less in the Lobe ejecta.

[49] The behavior of the GPR in detecting subsurface blocks in ejecta can be understood in the context of field observations of the subsurface, with the relations established here working toward characterizing the GPR signature of Meteor Crater ejecta. Down to depths of 1 m, there are typically an abundance of apparent block detections in GPR data, which are here found to overestimate the true block population. The likely reason for the overestimate is excess block-like detections due to the nature of the medium: densely packed with clasts of varying size and shape, which complicates the propagation and reflections of the radar waves. While interaction of these waves may create excess apparent block features in the data in the upper meter, the same effects of this highly scattering material reduce the ability to pick out blocks at greater depths, both by reducing power and contorting or masking block signatures.

[50] The greater overestimation of GPR counts in the Lobe ejecta compared with the Quarry ejecta reflects the field observations of the constituents and nature of fracturing of the two ejecta types. In the Lobe ejecta, blocks of multiple lithologies are present in a matrix of clasts of ever decreasing size, the result of fragmented blocks being completely separated from their neighbors and mixed with other fragments during the syn-impact ejection process. The Quarry ejecta is closer to the crater rim and is a more intact, coherent section of the overturned ejecta blanket, in which single-lithology large blocks are heavily fractured yet the fragments in the majority of cases remain in close contact with their parent neighbors. These individual fragments were counted in the visual size-frequency results. However, a fractured cluster may more likely appear to the GPR as a single block than a collection of fragments in the Lobe ejecta because the Quarry fragments are the same composition with little to no separation, displacement, or matrix fill between neighbors. Blocks are less well resolved from their background by GPR in the Quarry, due both to compositional homogeneity of the Coconino here and to gradational transitions in physical integrity of the blocks and pulverized sandstone, leading to fewer apparent detections and likely also fewer and weaker multiple reflections.

[51] The above relations between apparent GPR detections and ground-truth counts allow the GPR signature of the Meteor Crater ejecta population to be linked to the actual ejecta population. More concretely, comparison with actual subsurface block counts allows a scaling factor to be estimated from the ratio of GPR counts to visual counts. Specifically, we find that GPR detections within the upper meter are ~2.1–3.5x higher at 400 MHz and ~1.4–1.8x higher at 200 MHz. GPR detections in the second meter are ~0.6–1.0x of actual block counts. In a remote setting, a GPR radargram with no apparent layering, few ideal hyperbolic features, but clustered with concave-up features (as illustrated in Figures 3 and 12) likely represents a highly scattering subsurface. Counting the apparent block detections with similar methods as here will allow comparison to the apparent blocks per cubic meter determined consistently for Meteor Crater impact ejecta here (Figure 13 and Table 2), which represents a population of blocks derived from multiple-fragmentation processed, as described by the power exponents in Figure 11. Our data lend a metric to qualitative comparisons that may be made to determine if the remote subsurface also represents such a population. Additionally, applying scaling factors to the GPR counts, which are apparent detections within the complex, net radar response to the subsurface, can yield a closer estimate to the actual number of structural reflectors, or blocks. In ejecta materials that are expected to be of similar composition (e.g., entirely within a lava field, as opposed to at a geologic contact), it is likely more appropriate to use the Quarry scaling factors.

[52] As discussed in the introduction and methods, the dielectric of the remote surface will affect the measured GPR radargrams in terms of the meters of depth represented by 1 ns and the total penetration depth. Meteor Crater measurements reported here are obtained in a limestone- and quartzite-rich medium with dielectric of 3.5–5.2, which likely increases with depth. Much of planetary surfaces are volcanic basalts in which dielectric could easily be above 7, and iron-rich materials on Mars could push it up to 15 [*Paillou et al*., 2001; *Olhoeft*, 1998; *Heggy et al*., 2001; *Stillman and Olhoeft*, 2008; *Williams and Greeley*, 2004; *Pettinelli et al*., 2006], although extremely dry conditions may help to mediate this. Such conditions could restrict penetration depths at these wavelengths to 2–3 m, and in extreme cases down to ~1 m. Due to the highly scattering nature of the Meteor Crater ejecta subsurface, we observed few detections below 3 m and enough to discuss only above 2 m. This limited penetration in ejecta- and crater-related terrain may be expected, and also common on heavily cratered planetary surfaces [e.g., *Unrau et al*., 2010; *Heggy and Paillou*, 2006]. However, it means that only the upper meter or two may be useful in assessing block population, at 200–400 MHz wavelengths, and that a higher dielectric may not exclude the most useful depths. On the other hand, using longer wavelengths in such planetary cases would help mediate the problem of the high dielectric, albeit limiting the detection sensibility to a higher size range of blocks.

[53] GPR is beneficial in investigating crater ejecta characteristics, yet interpretation is challenging. There is a trade-off between attempting to detect a greater fraction of the population of rocks by using shorter wavelength GPR, and the increased scattering that occurs in the more subsurface objects is visible to the radar at shorter wavelength. In order to reduce such clutter, the use of a longer wavelength may serve to filter out the presence of the smaller blocks causing much of the clutter by effectively making them part of the background medium. This also has the advantage of greater depth penetration. The advantage of employing two antennas with different detection and penetration capabilities is that it provides two facets of characterization of a block population.

7. Conclusions

[54] Our work quantifies the GPR character of the Meteor Crater ejecta as reflected in the apparent distribution of blocks in the near surface. This GPR signature is linked, or ground truthed, to the actual block population by direct pit-wall observation, establishing a link between a radargram metric and a population of blocks produced by fragmentation during an impact ejection event. We find that GPR overestimates block counts in the upper meter, likely due to the clutter caused by scattering from the many closely spaced blocks typical of ejecta. In the upper meter, overestimation ranges from a factor of ~3.5 in a well-mixed ejecta, to ~2 in a lithologically homogeneous, less disrupted overturned ejecta; in the second meter, apparent GPR detections are 0.6–1.0x visual counts. In addition to attenuation with depth, the amount of scattering in the upper meter is likely the cause of lower than expected detections in the second and third meters. While the 200 MHz antenna made fewer detections than the 400 MHz, it may be better at filtering out the clutter caused by the many blocks at smaller sizes, due to its reduced resolution. In environments with higher dielectrics, expected in volcanic terrains and on Mars, longer wavelength GPR would be preferable. Use of two wavelengths and division into three depth zones provides multiple aspects of this characterization metric for Meteor Crater ejecta. With this study, GPR signatures of ejecta and other blocky environments for which no ground truth is available, as on the Moon or Mars, can be compared to these GPR results from Meteor Crater (i.e., Figures 11 and 13), thereby enabling relative inferences to be made about the actual size and depth distribution of blocks in the remote ejecta, relative to that of Meteor Crater. In addition, the consistent characterization of crater ejecta by its GPR apparent block metric serves as a comparative basis in recognizing remote populations of ejecta blocks and distinguishing them from products of fundamentally different geologic processes.

[55] **Acknowledgments.** Many thanks to D. Kring, B. Andes, and the Barringer family for access and guidance in performing research in the unique environment of Meteor Crater. Appreciation is given for the time taken by Gwen Bart and an anonymous reviewer for their helpful comments on the manuscript. This research was carried out as part of the NASA Lunar Science Institute team led by D. B. J. Bussey, Award #NNA09DB31A.

References

Baker, G. S., and H. M. Jol, Eds. (2007), *Stratigraphic Analyses Using GPR*, Geological Society of America Special Papers, *432*, 181 p., The Geological Society of America, Boulder, CO.

Baker, G. S., T. E. Jordan, and J. Pardy (2007), An introduction to ground penetrating radar (GPR), in *Stratigraphic Analyses Using GPR*, Geological Society of America Special Papers, *432*, edited by G. S. Baker, and H. M. Jol, pp. 1–18, doi:10.1130/2007.2432(01).

Barringer, D. M. (1905), Coon Mountain and Its Crater. Proceedings of the Academy of Natural Sciences of Philadelphia. 57, 861–886.

Bart, G. D., and H. J. Melosh (2007), Using lunar boulders to distinguish primary from distant secondary impact craters, *Geophys. Res. Lett*, *34*, L07203, doi:10.1029/2007GL029306.

Bart, G. D., and H. J. Melosh (2010), Distributions of boulders ejected from lunar craters, *Icarus*, *209*, 337–357.

Benson, A. K. (1995), Applications of ground penetrating radar in assessing some geological hazards: examples of groundwater contamination, faults, cavities, *J. Appl. Geophys.*, *33*(1–3), 177–193.

Berthelier, J. J., et al. (2003), GPR, a ground-penetrating radar for the Netlander mission, *J. Geophys. Res., 108*(E4), 8027, doi:10.1029/2002JE001866.

Binder, A. B., R. E. Arvidson, E. A. Guinness, K. L. Jones, T. A. Mutch, E. C. Morris, D. C. Pieri, and C. Sagan (1977), The geology of the Viking Lander 1 site, *J. Geophys. Res.*, *82*, 4439–4451, doi:10.1029/JS082i028p04439.

Brace, W. F. (1960), An extension of the Griffith theory of fracture to rocks, *J. Geophys. Res.*, *65*, 3477–3480, doi:10.1029/JZ065i010p03477.

Bristow, C. S., P. C. Augustinus, I. C. Wallis, H. M. Jol, and E. J. Rhodes (2010), Investigation of the age and migration of reversing dunes in Antarctica using GPR and OSL, with implications for GPR on Mars, *Earth Planet. Sci. Lett.*, *289*, doi:10.1016/j.epsl.2009.10.026.

Ciarletti, V., C. Corbel, D. Plettemeier, P. Cais, S. M. Clifford, and S.-E. Hamran (2011), WISDOM GPR Designed for Shallow and High-Resolution Sounding of the Martian Subsurface, *Proc. IEEE*, *99*, doi:10.1109/JPROC.2010.2100790.

Conyers, L. B. (2004), *Ground-penetrating radar for archaeology*, AltaMira Press, Walnut Creek, CA.

Daniels, D. J. (Ed) (2007), *Ground Penetrating Radar*, 2nd ed., IET Radar, Sonar, Navigation, and Avionics Series 15, 726 p., The Institution of Engineering and Technology, London.

Degenhardt, J. J., and J. R. Giardino (2003), Subsurface investigation of a rock glacier using ground-penetrating radar: Implications for locating stored water on Mars, *J. Geophys. Res.*, *108*(E3), 8036, doi:10.1029/2002JE001888.

Dinwiddie, C. L., R. N. McGinnis, D. E. Stillman, K. L. Bjella, and R. E. Grimm (2011), Geophysical Mars Analog Studies of Multiphase Water in the Great Kobuk Sand Dunes, Northwestern Alaska, 42nd Lunar Planet. Sci. Conf., Abstract #2501.

Dominic, D. F., K. Egan, C. Carney, P. J. Wolfe, and M. R. Boardman (1995), Delineation of shallow stratigraphy using ground penetrating radar, *J. Appl. Geophys.*, *33*(1–3), 167–175.

Fukui, K., T. Sone, J. A. Strelin, C. A. Toriell, J. Mori, and Y. Fujii (2008), Dynamics and GPR stratigraphy of a polar rock glacier on James Ross Island, Antarctic Peninsula, *J. Glaciol.*, *54*, doi:10.3189/002214308785836940.

Furgale, P., T. D. Barfoot, N. Ghafoor, K. Williams, and G. Osinski (2010), Field Testing of an Integrated Surface/Subsurface Modeling Technique for Planetary Exploration, *Int. J. Rob. Res.*, *29*, doi:10.1177/0278364910378179.

Gault, D. E., E. M. Shoemaker, and H. J. Moore (1963), Spray ejected from the lunar surface by meteoroid impact, NASA Tech Note D-1767, 39 p.

Gilbert, G. K., D. M. Barringer, H. L. Fairchild, G. P. Merrill, and W. H. Pickering (1896), Meteor Crater, Arizona.

Gilvary, J. J. (1961), Fracture of brittle solids. I. distribution function for fragment size in single fracture (theoretical), *J. Appl. Phys.*, *32*, 391.

Gilvary, J. J., and B. H. Bergstrom (1961), Fracture of brittle solids. II. distribution function for fragment size in single fracture (experimental), *J. Appl. Phys.*, *32*, 400.

Golombek, M., and D. Rapp (1997), Size-frequency distributions of rocks on Mars and Earth analog sites: Implications for future landed missions, *J. Geophys. Res.*, *102*(E2), 4117–4129.

Golombek, M. P., A. F. C. Haldemann, N. K. Forsberg-Taylor, E. N. DiMaggio, R. D. Schroeder, B. M. Jakosky, M. T. Mellon, and J. R. Matijevic (2003), Rock size-frequency distributions on Mars and implications for Mars Exploration Rover landing safety and operations, *J. Geophys. Res.*, *108*, 8086. doi:10.1029/2002JE002035.

Golombek, M. P., et al. (2006), Geology of the Gusev cratered plains from the Spirit rover transverse. *J. Geophys. Res.*, *111*, E22S07. doi:10.1029/2005JE002503.

Golombek, M. P., et al. (2008), Size-frequency distributions of rocks on the northern plains of Mars with special reference to Phoenix landing surfaces. *J. Geophys. Res.*, *113*, E00A09, doi:10.1029/2007JE003065.

Golombek, M., J. A. Huertas, D. Kipp, and F. Calef (2012), Detection and characterization of rocks and rock size-frequency distributions at the final four Mars Science Laboratory Landing Sites, *Mars: The International Journal of Mars Science and Exploration*, *7*, 1–22, doi:10.1555/mars.2012.0001.

Graham, L. D., T. G. Graff, and the 2012 MMAMA team (2013), Rover-Based Instrumentation and Scientific Investigations during the 2012 Analog Field Test on Mauna Kea Volcano, Hawaii. Lunar and Planetary Institute Science Conference 44, Abstract #2269.

Grant, J. A., and P. H. Schultz (1993), Erosion of ejecta at Meteor Crater, Arizona, *J. Geophys. Res.*, *98*, 15,033–15,047.

Grant, J. A., and P. H. Schultz (1994), Erosion of ejecta at Meteor Crater: Constraints from Ground Penetrating Radar, Proc. 5th Int. Conf. GPR, p. 789–803.

Grant, J. A., A. E. Schutz, R. E. Arvidson, and B. A. Campbell (2001), *Development and field testing of a rover-deployable ground penetrating radar*, EOS AGU Annual Fall Meeting, San Francisco, CA, P42A-0570.

Grant, J. A., A. E. Schutz, and B. A. Campbell (2003), Ground penetrating radar as a tool for probing the shallow subsurface of Mars, *J. Geophys. Res.*, *108*(E4), 8024, doi:10.1029/2002JE001856.

Grant, J. A., T. A. Maxwell, A. K. Johnston, A. Kilani, and K. K. Williams (2004), Documenting drainage evolution in Bir Kiseiba, southern Egypt: Constraints from ground-penetrating radar and implications for Mars. *J. Geophys. Res.*, *109*, 9002. doi:10.1029/2003JE002232.

Grant, J. A., S. A. Wilson, S. W. Ruff, M. P. Golombek, and D. L. Koestler (2006) Distribution of rocks on the Gusev Plains and on Husband Hill, Mars. *Geophys. Res. Lett.*, *33*, 16202. doi:10.1029/2006GL026964.

Griffith, A. A. (1921), The Phenomena of Rupture and Flow in Solids, *Royal Society of London Philosophical Transactions Series A*, *221*, 163–198, doi:10.1098/rsta.1921.0006.

Grimm, R. E., E. Heggy, S. Clifford, C. Dinwiddie, R. McGinnis, and D. Farrell (2006), Absorption and scattering in ground-penetrating radar: Analysis of the Bishop Tuff, *J. Geophys. Res.*, *111*, E06S02, doi:10.1029/2005JE002619.

Heet, T. L., R. E. Arvidson, S. C. Cull, M. T. Mellon, and K. D. Seelos (2009), Geomorphic and geologic settings of the Phoenix Lander mission landing site, *J. Geophys. Res.*, *114*, E00E04, doi:10.1029/2009JE003416.

Heggy, E., and P. Paillou (2006), Probing structural elements of small buried craters using ground-penetrating radar in the southwestern Egyptian desert: Implications for Mars shallow sounding, *Geophys. Res. Lett.*, *33*, L05202, doi:10.1029/2005GL024263.

Heggy, E., P. Paillou, G. Ruffie, J. M. Malezieux, F. Costard, and G. Grandjean (2001), On water detection in the martian subsurface using sounding radar, *Icarus*, *154*, doi:10.1006/icar.2001.6717.

Heggy, E., S. M. Clifford, R. E. Grimm, C. L. Dinwiddie, J. A. Stamatakos, and S. H. Gonzalez (2006a), Low-frequency radar sounding investigations of the North Amargosa Desert, Nevada: A potential analog of conductive subsurface environments on Mars, *J. Geophys. Res.*, *111*, E06S03, doi:10.1029/2005JE002523.

Heggy, E., S. M. Clifford, R. E. Grimm, C. L. Dinwiddie, D. Y. Wyrick, and B. E. Hill (2006b), Ground-penetrating radar sounding in mafic lava flows: Assessing attenuation and scattering losses in Mars-analog volcanic terrains, *J. Geophys. Res.*, *111*, E06S04, doi:10.1029/2005JE002589.

Hooper, D. M., C. L. Dinwiddie, R. N. McGinnis, K. J. Smart, and M. M. Roberts (2012), Observations of Debris Flows at the Great Kobuk Sand Dunes, Alaska: Implications for Analogous Features on Mars, 43rd Lunar and Planetary Science Conference, Abstract #2040.

Inglis, C. E. (1913), Stresses in a plate due to the presence of cracks and sharp corners, *Inst Naval Arch.*, *55*, 219–230.

Jol, H. M., Ed. (2009), *Ground Penetrating Radar: Theory and Applications*, 524 p.. Elsevier, Amsterdam.

Khan, S. D., E. Heggy, and J. Fernandez (2007), Mapping exposed and buried lava flows using synthetic aperture and ground-penetrating radar in Craters of the Moon lava field, *Geophysics*, *72*, doi:10.1190/1.2793298.

Kring, D. A. (2007), *Guidebook to the Geology of Barringer Meteorite Crater, Arizona*, 150 pp., LPI Contribution 1355, Houston, TX.

Kumar, P. S., J. W. Head, and D. A. Kring (2010), Erosional modification and gully formation at Meteor Crater, Arizona: Insights into crater degradation processes on Mars, *Icarus*, *208*, 608–620, doi:10.1016/j.icarus.2010.03.032.

LEAG (2009a), Community Forum on Future Lunar Science Missions at the Fortieth Lunar and Planetary Science Conference, Lunar Exploration Analysis Group (LEAG), 5 p. http://www.lpi.usra.edu/leag/reports.shtml.

LEAG (2009b), The Lunar Exploration Roadmap: Exploring the Moon in the 21st Century: Themes, Goals, Objectives, Investigations, and Priorities. 2009, v 1.0, Lunar Exploration Analysis Group (LEAG), 121 p. http://www.lpi.usra.edu/leag/ler_draft.shtml.

Leuschen, C., P. Kanagaratnam, K. Yoshikawa, S. Arcone, and P. Gogineni (2003a), Design and field experiments of a ground-penetrating radar for Mars exploration, *J. Geophys. Res.*, *108*(E4), 8034, doi:10.1029/2002JE001876.

Leuschen, C., S. Clifford, and P. Gogineni (2003b), Simulation of a surface-penetrating radar for Mars exploration, *J. Geophys. Res.*, *108*(E4), 8035, doi:10.1029/2002JE001875.

Mellet, J. S. (1995), Ground penetrating radar applications in engineering, environmental management, and geology, *J. Appl. Geophys.*, *33*(1–3), 157–166.

Melosh, H. (1989), *Impact Cratering: A geologic process*, Oxford monographs on geology and geophysics, no. *11*, 253 p., Oxford University Press, New York.

MEPAG (2008), *Mars Science Goals, Objectives, Investigations, and Priorities: 2008*, edited by J. R. Johnson, 37 p., white paper posted September, 2008 by the Mars Exploration Program Analysis Group (MEPAG), at http://mepag.jpl.nasa.gov/reports/index.html.

Milsom, J. (2003), *Field Geophysics*, John Wiley & Sons Ltd., West Sussex, pp. 232.

Moore, H. J., and J. M. Keller (1990), Surface-Material Maps of Viking Landing Sites on Mars. Reports of Geology and Geophysics Program 1989, *NASA Tech Memo*, *4210*, 533–535.

Moore, H. J., and J. M. Keller (1991), Surface-Material Maps of Viking Landing Sites on Mars. Reports of Geology and Geophysics Program 1990, *NASA Tech Memo*, *4300*, 160–162.

Mussett, A. E., and M. A. Khan (2000), *Looking into the Earth: An Introduction to Geological Geophysics*, 470 p., Cambridge Univ. Press, Cambridge.

Nishiizumi, K., C. P. Kohl, J. R. Arnold, E. M. Shoemaker, J. Klein, D. Fink, and R. Middleton (1991), In situ Be-10-Al-26 exposure ages at Meteor Crater, Arizona, *Geochim. Cosmochim. Acta*, *55*, 2699–2703, doi:10.1016/0016-7037(91)90388-L.

Olhoeft, G. R. (1998), Ground penetrating radar on Mars, Proc. of Seventh Int'l. Conf. on Ground Penetrating Radar, Lawrence, KS, p. 387–392.

Paillou, P., G. Grandjean, J. M. Malezieux, G. Ruffie, E. Heggy, D. Piponnier, P. Dubois, and J. Achache (2001), Performances of Ground Penetrating Radars in arid volcanic regions: Consequences for Mars subsurface exploration, *Geophys. Res. Lett.*, *28*, doi:10.1029/1999GL008449.

Pettinelli, E., et al. (2006), Electromagnetic propagation features of ground-penetrating radars for the exploration of Martian subsurface, *Near Surface Geophysics*, *4*, 5–11.

Pettinelli, E., P. Burghignoli, A. R. Pisani, F. Ticconi, A. Galli, G. Vannaroni, and F. Bella (2007), Electromagnetic propagation of GPR signals in Martian subsurface scenarios including material losses and scattering, *IEEE Trans. Geosci. Remote Sens.*, *45*, doi:10.1109/TGRS.2007.893563.

Roddy, D. J., J. M. Boyce, G. W. Colton, and A. L. Dial Jr. (1975), Meteor Crater, Arizona, rim drilling and thickness, structural uplift, diameter, depth, volume, and mass-balance calculations, Proc. 6th Lunar Science Conf., p. 2621–2644.

Russell, P. S., J. A. Grant, K. K. Williams, L. M. Carter, W. B. Garry, G. Morgan, I. Daubar, and D. B. J. Bussey (2012), Ground Penetrating

Radar Field Studies of Lunar-Analog Geologic Settings: Impact Ejecta and Volcanic Materials. Lunar and Planetary Institute Science Conference 43, Abstract #2604.

Shearer, C., et al. (2004), Findings of the Moon_Mars Science Linkage Science Steering Group, Mars Exploration Program Analysis Group (MEPAG), 29 p. http://mepag.jpl.nasa.gov/reports/index.html.

Shoemaker, E. M. (1960), Intl. Geol. Congress, Rept. 18, 418–434.

Shoemaker, E. M. (1963), Impact Mechnics at Meteor Crater, Arizona, in *The Moon, Meteorites, and Comets*, edited by B. M. Middlehurst and G. P. Kuiper, pp. 301–336, Univ. Chicago Press, Chicago.

Shoemaker, E. M., and S. W. Kieffer (1974), *Guidebook to the Geology of Meteor Crater, Arizona*, Center for Meteorite Studies, Arizona State University, Tempe, pp. 66, Government Printing Office, Washington, DC.

Shoemaker, E. M., and E. C. Morris (1969), *Size-frequency distribution of fragmental debris, in Surveyor Program Results*, NASA Special Publication SP-184, pp. 82–96, Government Printing Office, Washington, D. C.

Soldovieri, F., G. Prisco, and S.-E. Hamran (2009), A preparatory study on subsurface exploration on Mars using GPR and microwave tomography, *Planet. Space Sci.*, *57*, doi:10.1016/j.pss.2008.11.014.

Steacy, S. J., and C. G. Sammis (1992), A damage mechanics model for fault zone friction, *J. Geophys. Res.*, *97*(B1), 587–594, doi:10.1029/91JB02338.

Stillman, D., and G. Olhoeft (2008), Frequency and temperature dependence in electromagnetic properties of Martian analog minerals, *J. Geophys. Res.*, *113*, E09005, doi:10.1029/2007JE002977.

Thomson, L. I., G. R. Osinski, and W. H. Pollard (2012), The dielectric permittivity of terrestrial ground ice formations: Considerations for planetary exploration using ground-penetrating radar, *J. Geophys. Res.*, *117*, E09003, doi:10.1029/2012JE004053.

Turcotte, D. L. (1992), *Fractals and Chaos in Geology and Geophysics*, 221 p., Cambridge University Press, Cambridge.

Unrau, T., K. F. Tiampo, R. G. Pratt, and G. Osinski (2010), A Ground Penetrating Radar Lunar Analogue Field Campaign in the Haughton Impact Structure, Canada, AGU Fall, Abstract #P23A-1619.

Valerio, G., A. Galli, P. M. Barone, S. E. Lauro, E. Mattei, and E. Pettinelli (2012), GPR detectability of rocks in a Martian-like shallow subsoil: A numerical approach, *Planet. Space Sci.*, *62*, doi:10.1016/j.pss.2011.12.003.

Vannaroni, G., et al. (2004), MUSES: multi-sensor soil electromagnetic sounding, *Planet. Space Sci.*, *52*, doi:10.1016/j.pss.2003.07.003.

Weibull, W. (1939), A statistical theory of the strength of materials. Proc. The Royal- Swedish Institute for Engineering Research. Nr. 151.

Williams, K. K., and R. Greeley (2004), Measurements of dielectric loss factors due to a Martian dust analog, *J. Geophys. Res.*, E10006, doi:10.1029/2002JE001957.